Final state interactions in three-meson systems: Analysis of data on $\bar{p}p \to \pi^0\pi^0\pi^0$ and $\eta\eta\pi^0$ at rest

V. V. Anisovich,[1,2,*], D. V. Bugg,[1,†] A. V. Sarantsev,[1,2,‡] and B. S. Zou[1,§]
[1]*Queen Mary and Westfield College, London E1 4NS, United Kingdom*
[2]*St. Petersburg Nuclear Physics Institute, Gatchina, St. Petersburg district, 188350 Russia*
(Received 19 January 1994)

We provide a theoretical and computational formalism for the study of three-body annihilation of $p\bar{p}$. It includes (i) an analysis of three-body equations with the purpose of extracting the leading singularities and (ii) an analysis of low-energy $\pi\pi$, $K\bar{K}$, $\eta\eta$, and $\pi\eta$ amplitudes and the reconstruction of them from available experimental data. Based on this formalism, we perform an analysis of data on $p\bar{p} \to \pi^0\pi^0\pi^0$ and $\eta\eta\pi^0$ at rest. The data are fitted well by pure $^1S_0$ annihilation and require two $I=0, J^{PC}=0^{++}$ resonances with $M_1=1335\pm40$ MeV, $\Gamma_1=255^{+60}_{-40}$ MeV, and $M_2=1505\pm20$ MeV, $\Gamma_2=150\pm20$ MeV. The latter explains features of the data previously interpreted in an alternative way as due to $A_X(1515)$ with $J^{PC}=2^{++}$. As a second step, we evaluate the magnitude of the amplitudes due to triangle singularities which result from rescatterings of outgoing mesons. Taking into account these rescattering processes enhances the magnitudes of low-lying resonances, notably $f_0(975)$.

PACS number(s): 13.75.Cs, 14.40.Cs

I. INTRODUCTION

High quality data on $\bar{p}p$ and $\bar{p}n$ annihilation into mesons are available now [1] and are becoming a valuable source of information about meson interactions at low and intermediate energies. Here we discuss the possibility of extracting precise information about meson-meson amplitudes from reactions of three-meson annihilation. This extraction is based on exploiting the conditions imposed by three-body unitarity and analyticity.

The principal features of the three-body problem, and its relation to constraints from unitarity and analyticity were discussed in the 1960s (see Refs. [2–7] and references therein). However this knowledge has not been turned to practical everyday use except in some special cases. Examples of exceptions are (i) the nonrelativistic Faddeev equation and (ii) three-body potential models with very specific choice of the potential, as in the Isgur-Karl model for baryons [8]. Relativistic three-body equations, being a generalization of the two-body N/D formalism [9], are rather cumbersome and do not allow easy extraction of information. Several attempts have been made to look for specific effects in three-body interactions, for example, the so-called triangle singularity (see discussion in Refs. [10–12]).

The appearance of high-quality data on $\bar{p}p$ (at rest) $\to \pi^0\pi^0\pi^0$ [13], $\eta\eta\pi^0$ [14], $\eta\pi^0\pi^0$ and related charged channels provides a good opportunity to extract information about interactions in $\pi\pi$, $\pi\eta$, and $\eta\eta$ channels. In publications so far [13,14] the analysis has been based on a simple isobar model. However, for these high-quality data this model is too simple. We mention a few examples of refinements which need to be taken into consideration. (1) The three-particle unitarity condition complicates matters: for example, it leads to the possibility of rescattering and results not only in triangle singularities but also in additional imaginary parts. (2) Much is known about $\pi\pi$ elastic scattering and $\pi\pi \to K\bar{K}$ from earlier experiments. The question arises how to incorporate this information into the analysis of three-body channels. In the simple isobar analysis, only the $\pi\pi \to \pi\pi$ amplitude was introduced with a constant complex coupling parameter Λ. However, over the wide mass range up to 1.74 GeV covered by the data we wish to discuss, this amplitude is built from a number of resonances i, which may have different coupling parameters Λ_i to the $\bar{p}p$ channel. This suggests the need for s dependence of coupling parameters. (3) It is also necessary to consider coupling via intermediate $K\bar{K}$ states. (4) There may also be background nonresonant contributions, and inelastic coupling to 4π. In order to address these problems we arrive at a more flexible form for $\pi\pi$ (and $\eta\eta$ and $\eta\pi$) amplitudes.

We first discuss the theoretical foundations for extracting leading singularities. This leads to an N/D formalism where two-meson resonances in the final state appear explicitly in D functions which are identical for both two- and three-meson channels. The N function contains left-hand singularities and may in principle be a complicated function of s. Indeed we point to data of Bettini *et al.* [15] which suggest strongly that this is the case.

In Sec. III, we discuss the implications of those data and then apply the ideas of Sec. II to a reanalysis of published Crystal Barrel data. A brief account of this work has already been presented by Anisovich *et al.* [16] and at the NAN [17] and Marseilles conferences [18]. We find evidence for two resonances $f_0(1335)$ and $f_0(1505)$ with quantum numbers $I=0 J^{PC}=0^{++}$ in $\pi^0\pi^0$ and $\eta\eta$ channels. Data on $\bar{p}p \to 3\pi^0$ and $\eta\eta\pi^0$ are consistent in masses and widths for these two resonances. In the published work of Ref. [13], the first of these resonances was

*Electronic address: ANISOVIC@LNPI.SPB.SU
†Electronic address: DVB@IB.RL.AC.UK
‡Electronic address: VSV@HEP486.LNPI.SPB.SU
§Electronic address: ZOU@V2.RL.AC.UK

overlooked and the second was interpreted in an alternative way as the $A_X(1515)$ resonance having $I=0J^{PC}=2^{++}$. This alternative requires 60% P-state annihilation in $\bar{p}p \to 3\pi^0$.

Section IV discusses triangle singularities and Sec. V evaluates their effect in first approximation. It turns out that their impact on resonance masses and widths lies within the errors attributable to other systematic effects. However, the inclusion of rescattering diagrams leads to a better resolution of low-energy resonances. Coupling parameters Λ_i, are perturbed by significant amounts, particularly their phases.

In Sec. VI we comment on the physics of $f_0(1335)$ and $f_0(1505)$. The former is a natural candidate for the ground-state nonet. There are other experiments in which $f_0(1505)$ appears. We put together a tentative case for interpreting $f_0(1505)$ as a glueball, with some $\bar{q}q$ mixing.

II. ANALYTIC STRUCTURE OF THE AMPLITUDE FOR $\bar{p}p \to$ THREE MESONS

Let us begin by considering an example where a spinless bound particle (the analogue of the $\bar{p}p$ bound state) decays to three spinless particles 1, 2, and 3. In this example we suppose there are no transitions via other intermediate states (e.g., $K\bar{K}$) or via intermediate states involving more than three mesons. This is a simplification which does not ultimately affect the form of the leading singularities.

The amplitude of the decay process is then determined by a direct transition [Fig. 1(a)] and subsequent rescatterings of final state particles [Figs. 1(b)–1(e) and so on]. For simplicity we consider here the case when the direct transition [Fig. 1(a)] does not depend on energies of final state particles and when rescatterings occur in S waves. This case reveals all the principal points needed for our considerations.

The amplitude A for three-particle production is then a sum of four blocks: (1) the direct production amplitude λ; (2) the amplitude $A_{12}(s_{12})$ where the last interaction is between particles 1 and 2 [for example, Figs. 1(b) or 1(e) with $i=1,k=2$]; similar amplitudes arise (3) with the last interaction between particles 1 and 3, $A_{13}(s_{13})$; and (4) with the last interaction between 2 and 3, $A_{23}(s_{23})$. Here s_{ik} is the two-particle invariant mass squared $s_{ik}=(p_i+p_k)^2$. So

$$A=\lambda+A_{12}(s_{12})+A_{13}(s_{13})+A_{23}(s_{23})\ . \tag{1}$$

The equation for amplitude $A_{12}(s_{12})$ is shown in graphical form in Fig. 2. In the nonrelativistic limit, it is the Faddeev equation. However, the relativistic generalization is ambiguous: it depends on the techniques used for writing the equation. Here we use the dispersion relation technique introduced for the three-body problem in Ref. [2] and discussed in a series of papers [5–7]. The dispersion relation technique in the nonrelativistic limit was applied in Ref. [19] to the three-nucleon problem and here we follow these ideas.

A. Two-particle scattering

As a first step we fix our technique for two-particle scattering amplitudes. We relate the standard N/D method [9] to the graphical technique of Ref. [20]. The partial wave scattering amplitude is written as a series of dispersion relation diagrams (Fig. 3) with different numbers of scatterings. Here the loop in Fig. 3(e) is equal to

$$b(s)=\int_{(m_i+m_k)^2}^{\infty}\frac{ds'}{\pi}\frac{G^R(s')\rho_{ik}(s')G_L(s')}{s'-s}\ , \tag{2}$$

where ρ is the two-particle phase-space factor

$$\rho_{ik}(s)=\frac{1}{16\pi s}\sqrt{[s-(m_i+m_k)^2][s-(m_i-m_k)^2]}\ ; \tag{3}$$

G^R and G_L are vertex functions which determine the particle interactions to right and left of Fig. 3(b). As a detail, G^R and G_L may be different. For the virtual processes the vertex functions are described by

$$G_L(s')G^R(s'')=V(s',s'') \tag{4}$$

since energy conservation applies only for initial and final states.

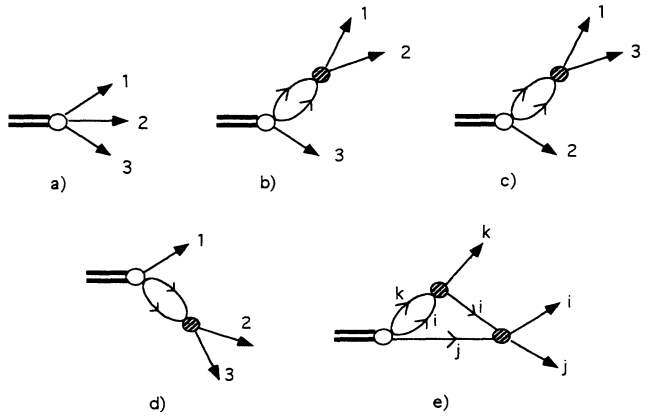

FIG. 1. Diagrams for the transition "bound particle→three mesons"; (a) direct production, (b)–(d) production with single rescattering, (e) production with double rescattering.

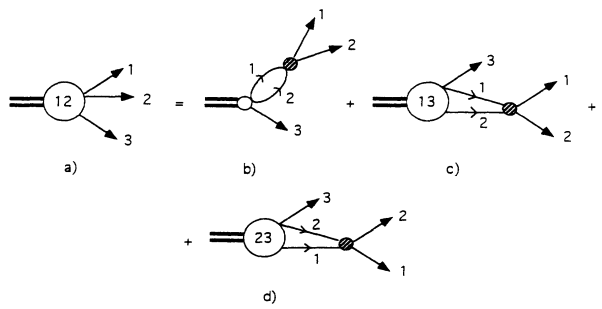

FIG. 2. The graphical form of the equation for the amplitude $A_{12}(s_{12})$ [block (a) in this figure].

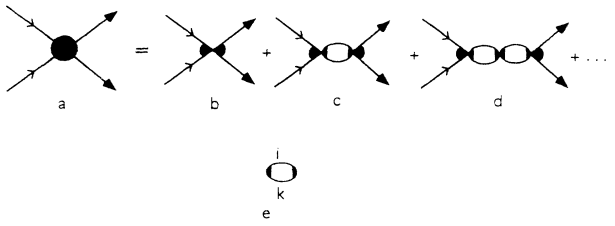

FIG. 3. The expansion of the scattering amplitude (a) as a series of rescattering diagrams [(b),(c),(d) $\cdots$]; (e) loop diagram defined by Eq. (2).

The series of Fig. 3 is given by

$$a(s)=G_L(s)G^R(s)+G_L(s)b(s)G^R(s)+G_L(s)b^2(s)G^R(s)+\cdots=\frac{G_L(s)G^R(s)}{1-b(s)}\ . \tag{5}$$

It is the partial scattering amplitude of the N/D method when Castilejo-Dyson-Dalitz (CDD) poles [21] are neglected: $G_L(s)G^R(s)$ is the N function, $N(s)$, while $D(s)=1-b(s)$. In the general case, the N function can be written as a sum of vertices:

$$N(s)=\sum_n G_L^{(n)}(s)G^R_{(n)}(s)\ . \tag{6}$$

The N function contains left-hand singularities related to t-channel exchange diagrams. For example, the s-channel partial wave of the diagram of Fig. 4(a) has a left-hand singularity at $s=4m^2-\mu^2$ (we put here $m_1=m_2=m_3=m_4=m$), while the diagram of Fig. 4(b) gives a branch cut starting at $s=4m^2-(2\mu)^2$, and so on. So the products G_LG^R in Eq. (6) have these singularities as well. From a consideration of the scattering amplitude, $a(s)$ of Eq. (5), it is not specified whether both vertices G_L and G^R have these singularities or only one vertex (G_L or G^R). It is easy to see that in the three-body problem the vertex $G^R(s)$ should be analytic. To see this, consider the case when the singularities of the N function are determined by the diagram of Fig. 4(a) and the amplitude for direct production, Fig. 4(c) is pointlike ($\lambda=$const). The amplitude with one rescattering of particles 1 and 2 is shown in Fig. 4(d). It has on the first sheet of the complex s_{12} plane only a singularity at $s_{12}=4m^2$. The corresponding dispersion relation diagram is equal to $b^\lambda_{12}(s_{12})G^R_{12}(s_{12})$, where the suffix λ denotes that b_{12} is associated with Fig. 4(c). This expression means that $G^R_{12}(s_{12})$ does not contain left-hand singularities. The simplest choice, which we will use, is

$$G^R(s)=1\ . \tag{7}$$

The asymmetry between $G^R(s)$ and $G_L(s)$, which does contain left-hand singularities, arises because the amplitude of the process "$\bar{p}p\to$three mesons" is not symmetric as well, see Fig. 5(a).

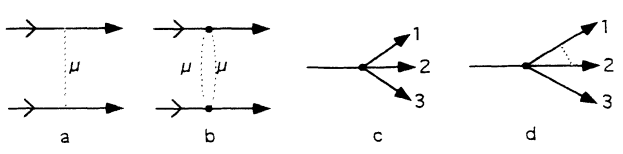

FIG. 4. Four-point diagrams with t-channel meson exchange in scattering process (a), (b), and in the three-particle production amplitude (d); direct production (c).

B. Three-particle scattering

Now let us write the equation for $A_{12}(s_{12})$ of Fig. 2. The diagram of Fig. 2(b) may be expressed as shown in Fig. 5(b) with the result

$$A^{2b}_{12}(s_{12})=\frac{b^\lambda_{12}(s_{12})G^R_{12}(s_{12})}{1-b_{12}(s_{12})} \tag{8}$$

and $b_{12}(s_{12})$ is displayed in Fig. 5(a):

$$b^\lambda_{12}(s_{12})=\int_{(m_1+m_2)^2}^\infty \frac{ds'}{\pi}\frac{\lambda\rho_{12}(s')G_L(s')}{s'-s_{12}}\ . \tag{9}$$

Here $[1-b_{12}(s_{12})]$ is exactly the same D function as that in the two-body scattering amplitude for channel 12.

Next the amplitude of Fig. 2(c) is

$$A^{2c}_{12}(s_{12})=\frac{B_{12}(s_{12})G^R_{12}(s_{12})}{1-b_{12}(s_{12})}\ , \tag{10}$$

where $B_{12}(s_{12})$ is shown diagrammatically in Fig. 6. The vital result for data analysis is that this amplitude and all contributions to $A_{12}(s_{12})$ contain the factor $[1-b_{12}(s_{12})]^{-1}$, due to final state interactions of particles 1 and 2. We can write

$$A_{12}(s_{12})=\frac{b^\lambda_{12}(s_{12})+B_{12}(s_{12})}{1-b_{12}(s_{12})}\ , \tag{11}$$

where Eq. (7) has been used. The denominators of Eq. (11) and the two-body amplitude, Eq. (5) are identical. This leads to the possibility of extracting two-body interactions from three-particle production data.

The full amplitude, Eq. (1), for three-particle production becomes

$$A=\lambda+\frac{b^\lambda_{12}(s_{12})+B_{12}(s_{12})}{1-b_{12}(s_{12})}+\frac{b^\lambda_{13}(s_{13})+B_{13}(s_{13})}{1-b_{13}(s_{13})}+\frac{b^\lambda_{23}(s_{23})+B_{23}(s_{23})}{1-b_{23}(s_{23})}\ . \tag{12}$$

The denominators contain two types of leading singulari-

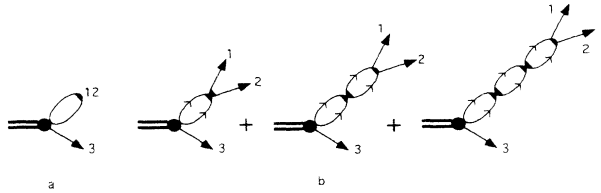

FIG. 5. The three-particle production block which includes interactions of particles 1 and 2 only.

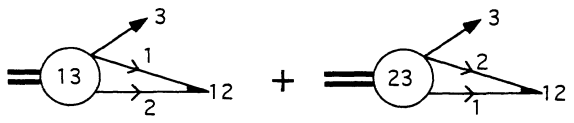

FIG. 6. The amplitude $B_{12}(s_{12})$.

ties: (i) poles, which are responsible for production of bound states or resonances, and may contain CDD poles from the $\bar{q}q$ system; (ii) two-particle threshold factors which can produce cusps. However, the numerators of Eq. (12), $b_{ik}^{\lambda}(s_{ik})+B_{ik}(s_{ik})$, also contain threshold singularities as well as the so-called triangle diagram singularities [22–24]. So we need to turn to a more detailed consideration of the amplitude $B_{ik}(s_{ik})$, which will be needed in Sec. IV.

C. $B_{ik}(s_{ik})$

The graphical representation of the block $B_{12}(s_{12})$ is given in Fig. 6. This equation may be written in the form of a dispersion integral:

$$B_{12}(s_{12}) = \int_{(m_1+m_2)^2}^{\infty} \frac{ds'}{\pi} \frac{G_L(s')\rho_{12}(s')}{s'-s_{12}} [\bar{A}_{13}(s')+\bar{A}_{23}(s')] . \tag{13}$$

Here

$$\bar{A}_{i3}(s') = \int_{C(i3)} \frac{dz_{i3}}{2} A_{i3}(s_{i3}), \quad i=1,2 , \tag{14}$$

where $z_{i3}=\cos\theta_{i3}$ in the enter of mass of particles 1 and 2. The contour of integration $C(i3)$ will be given below after writing out kinematical relations:

$$\begin{aligned} s_{13} &= m_1^2+m_3^2-2p_{10}^* p_{30}^* + 2z_{13}p_1^* p_3^* , \\ p_{10}^* &= \frac{s'+m_1^2-m_2^2}{2\sqrt{s'}}, \quad p_1^* = \sqrt{p_{10}^{*2}-m_1^2} , \\ p_{30}^* &= \frac{s'+m_3^2-s}{2\sqrt{s}}, \quad p_3^* = \sqrt{p_{30}^{*2}-m_3^2} . \end{aligned} \tag{15}$$

Then s_{23} is obtained from Eq. (15) by the replacement $1 \leftrightarrow 2$ and $z_{13} \leftrightarrow -z_{23}$; s is the total energy squared of particles 1, 2, and 3 (or the mass squared of the initial bound state):

$$s+m_1^2+m_2^2+m_3^2 = s_{12}+s_{23}+s_{13} .$$

The contour integration $C(i3)$ at small s',

$$\begin{aligned} (m_1+m_3)^2 \le s' &\le \frac{m_i s}{m_i+m_3} + \frac{m_3}{m_i+m_3}(m_1+m_2-m_i)^2 \\ &\quad - m_i m_3 \\ &\equiv s(0) , \end{aligned} \tag{16}$$

coincides with the phase space integration contour

$$-1 \le z_{i3} \le 1 . \tag{17}$$

It is denoted in Fig. 7(a) by a solid line I. But at

$$s(0) < s' < (\sqrt{s}-m_3)^2 , \tag{18}$$

the contour $C(i3)$ contains an additional piece shown in Fig. 7(a) by the dashed line (II). This piece of the integration was missed in Refs. [2,3]. At $s' > (\sqrt{s}-m_3)^2$, the integration in Eq. (14) is performed in the complex s_{i3} plane, Fig. 7(b).

Equations (12) and (13) apply to an S-wave two-particle interaction. Equations for $L \ge 1$ are given in Ref. [25].

D. Relation to Breit-Wigner amplitudes

Up to now we have discussed the interaction $V(s',s'')$ which does not contain poles. Poles in the scattering amplitude may appear in this case as zeros of the D function: $1=b_{ij}(s_{ij})$. These poles correspond to composite states of particles i and j. However the amplitude may contain resonances which are not such type of composite systems but have another origin (for example, resonances related to $q\bar{q}$ bound states or glueballs). In these cases,

$$V(s',s'') = g_L(s') \frac{1}{M^2-s_{ik}} g^R(s'') . \tag{19}$$

This term corresponds to the diagram of Fig. 8(a) if $s'=s''=s_{ik}$. The series of diagrams in Fig. 8 gives

$$\begin{aligned} a(s_{ik}) &= \frac{g_L(s_{ik})g^R(s_{ik})}{M^2-s_{ik}} \left[1-\frac{b(s_{ik})}{M^2-s_{ik}}\right]^{-1} \\ &= \frac{g_L(s_{ik})g^R(s_{ik})}{M^2-s_{ik}-b(s_{ik})} \end{aligned} \tag{20}$$

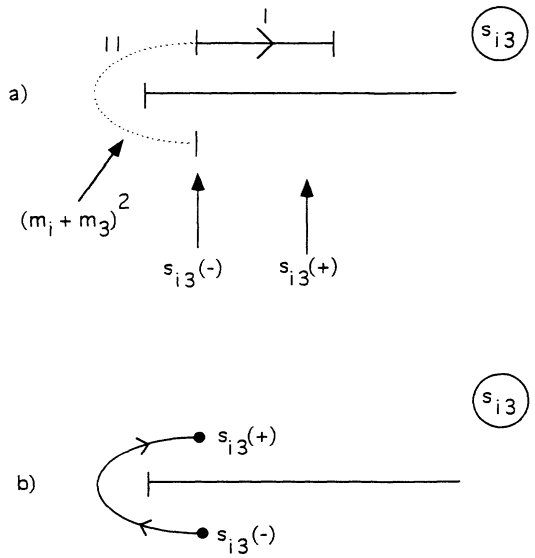

FIG. 7. Contour integration $C(i3)$ in the complex plane s_{i3}; $s_{i3}(+)$ and $s_{i3}(-)$ are determined by Eq. (15) at $z_{i3}=\pm 1$, respectively.

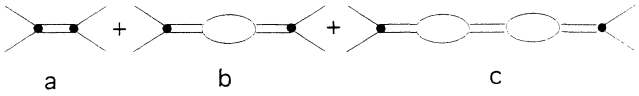

FIG. 8. The loop diagram $b(s_{ik})$.

with

$$b(s_{ik})=\int_{(m_i+m_k)^2}^{\infty}\frac{ds'}{\pi}\frac{g^R(s')\rho_{ik}(s')g_L(s')}{s'-s_{ik}}\ , \tag{21}$$

where $b(s_{ik})$ is the loop diagram in Fig. 8.

The standard Breit-Wigner formula corresponds to neglecting the energy dependence in $g^2(s_{ik})$ and $b(s_{ik})$:

$$a(s_{ik})=\frac{g_L(M_0^2)g^R(M_0^2)}{M_0^2-s_{ik}-i\Gamma M_0}\ , \tag{22}$$

where

$$M_0^2=M^2-\mathrm{Re}b(M_0^2)\ , \tag{23}$$

$$\Gamma=g^R(M_0^2)\rho_{ik}(M_0^2)g_L(M_0^2)\ . \tag{24}$$

A more sophisticated Breit-Wigner formula which takes into account the two-particle threshold behavior is

$$\Gamma=g^R(s_{ik})\rho_{ik}(s_{ik})g_L(s_{ik})\ . \tag{25}$$

The three-particle amplitude is written in an analogous way illustrated in Fig. 9. Again the amplitude $A_{ik}(s_{ik})$ contains the same resonance denominators:

$$A_{ik}(s_{ik})=\frac{g_{ik}^R(s_{ik})}{M_0^2-s_{ik}-i\Gamma M_0}[\lambda_R+b_{ik}^{\lambda}(s_{ik})+B_{ik}(s_{ik})]\ . \tag{26}$$

The more general case, when the two-particle interaction is a sum of resonance and nonresonance terms, can be considered similarly:

$$V(s',s'')=\frac{g_L(s')g^R(s'')}{M^2-s_{ik}}+G_L(s')G^R(s'')\ . \tag{27}$$

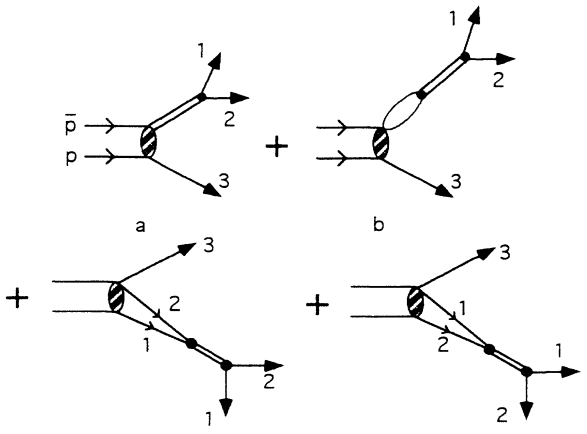

FIG. 9. The three-particle amplitude.

In this case, the blocks $A_{ik}(s_{ik})$ of Eq. (1) have a structure

$$A_{ik}(s_{ik})=\frac{\alpha_{ik}(s_{ik})}{[M^2-s_{ik}-b_{gg}(s_{ik})][1-b_{GG}(s_{ik})]+b_{gG}^2(s_{ik})}\ . \tag{28}$$

The denominator on the right-hand side is just the same as in the two-body scattering amplitude $i+k\to i+k$. In an analogous way we can treat cases when scattering amplitudes $i+k\to i+k$ contains two or more resonances.

III. FITS TO DATA

In Figs. 10 and 11 we reproduce published Crystal Barrel data sets on $\bar{p}p\to\pi^0\pi^0\pi^0$ [13] and $\eta\eta\pi^0$ [14] at rest. This group has also presented data on $\bar{p}p\to\eta\pi^0\pi^0$ at many conferences. Our methods apply equally well to these data, but presently we do not have access to them. First we discuss qualitative features of the data in order to provide a perspective to our fits.

Figure 10 has sixfold symmetry, because of the three identical π^0. There are three distinct features. Firstly, there are strong peaks at the edges of the Dalitz plot due to $f_2(1270)$. Secondly, there is a deep hole at the center of the plot. The Crystal Barrel Collaboration interpreted it as evidence for strong P-state annihilation, since annihilation from an initial $^3P_2$ state gives a zero there if the final state is governed purely by phase space. Thirdly, there is a complicated structure near 1515 MeV, interpreted in [13] as $A_X(1515)$ with $J^{PC}=2^{++}$, and produced largely from initial $^3P_1$ and $^3P_2$ states. The fit to the data led to the surprising conclusion that $\sim 60\%$ of annihilation is from initial P states.

We favor a quite different interpretation of the data. The motivation arises in the Veneziano model and the in-

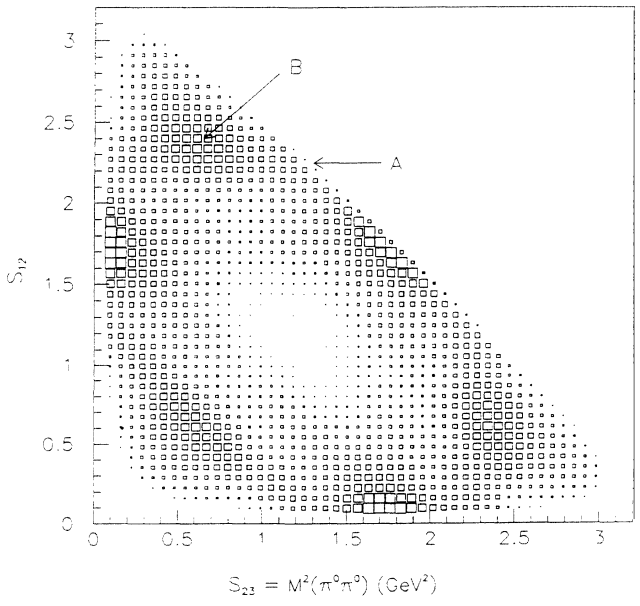

FIG. 10. Dalitz plot for $\bar{p}p\to 3\pi^0$ at rest, reproduced from Ref. [13].

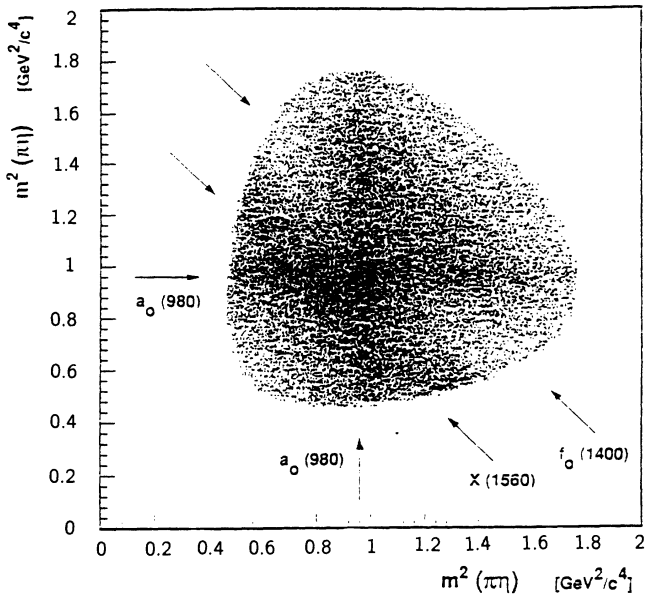

FIG. 11. Dalitz plot for $\bar{p}p \to \eta\eta\pi^0$ at rest, reproduced from Ref. [14].

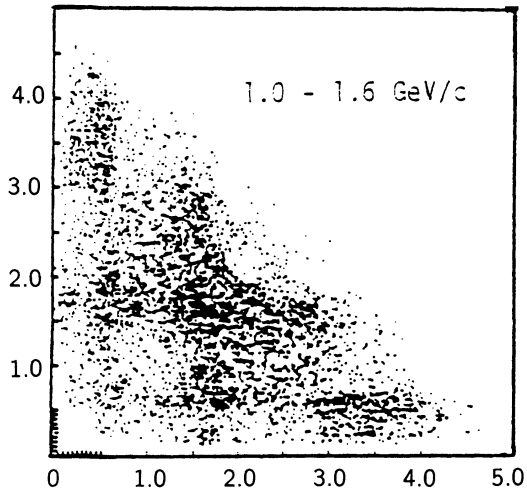

FIG. 13. Data of Bettini *et al.* on $\bar{p}n \to \pi^-\pi^+\pi^-$ at 1.6 GeV, reproduced from Ref. [15], Fig. 20.

cisive paper of Lovelace [26] on $\bar{p}n \to \pi^-\pi^+\pi^-$. In the Veneziano model, there are regularly spaced towers of resonances starting with $\rho(770)$ and $f_2(1270)$. The intersections of f_2 resonances in channels 12, 23, and 13 lead to Odorico zeros [27] running through the intersections. In Fig. 12 we suggest that these zeros, shown dashed, propagate across the Dalitz plot, through the central hole to the Adler zeros near the corners of the plot. This gives a dynamical explanation of the central dip. Lovelace showed that annihilation from the $^1S_0$ initial state gives a qualitative explanation of $\bar{p}n \to \pi^-\pi^+\pi^-$ data at rest, a channel closely related to $\bar{p}p \to 3\pi^0$ since they share $I=1$.

The data of Bettini *et al.* [15] at 1.6 GeV are reproduced in Fig. 13. One sees a regular lattice of peaks and dips, regularly spaced in s, t, and u. The hole at the center of Fig. 10 in data at rest coincides with one of the dips, at $s \simeq 1.1$ GeV^2, suggesting that this dip is not due to $^3P_2$ annihilation.

In the $\pi^-\pi^+\pi^-$ data discussed by Lovelace, $\rho(770)$ plays a strong role. However, we are dealing in Fig. 10 with $3\pi^0$ data, where $\rho(770)$ is absent. Near 800 MeV, the $\pi\pi$ S-wave phase shift δ_S also rises slowly through 90°, Fig. 14(a), giving the intensity distribution of Fig. 14(b). The peak at 800 meV is what we shall call the "σ" resonance, for brevity. We suggest that the zeros of Fig. 12 propagate through the intersections of σ bands. We shall show that the intersecting σ bands account for the bumps labeled B in Fig. 10 at $s \simeq 0.64$ GeV^2.

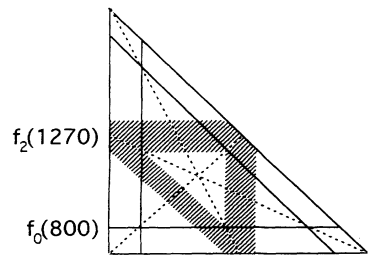

FIG. 12. Schematic diagram showing poles and zeros in $\bar{p}p \to 3\pi^0$. Dashed lines show our suggestion for zero trajectories.

Although our considerations are motivated by the Veneziano model we have found that doing actual fits with Veneziano amplitudes is cumbersome and fraught with problems. The algebraic forms we use, described below, are simpler, but allow the sort of mass dependence intrinsic to the Veneziano model.

Next we turn to the $\eta\eta\pi^0$ data of Fig. 11. There are three essential features. Firstly, there are horizontal and vertical bands due to $a_0(980)$ in $\eta\pi$. Secondly, there are diagonal bands ascribed in Ref. [14] to $f_0(1430)$ and $f_0(1560)$ in $\eta\eta$. Thirdly, there is a significant dip separating these two diagonal bands. These features lead us to ask whether these f_0 resonances are also present in $3\pi^0$ data. Our answer is essentially yes, though the higher quality $3\pi^0$ data lead to somewhat lower masses for both resonances. We shall show that the band marked A in Fig. 10 may be explained by a 0^{++} resonance with mass 1505 ± 20 MeV, $\Gamma=150\pm20$ MeV. In $\eta\eta\pi^0$, we find a lower mass for this resonance than given in Ref. [14]. The reason is that the $a_0(980)$ resonance was fitted in [14] by a simple Breit-Wigner amplitude. We replace it with a Flatté form [28] which takes into account the cusp at the $K\bar{K}$ threshold. The long tail of the Flatté form introduces interferences with $\eta\eta$ amplitudes and shifts the masses of $\eta\eta$ resonances significantly. Using this form, the higher of the two $\eta\eta$ resonances fits naturally to a mass of 1512 MeV, $\Gamma=158$ MeV, compatible within errors with the fitted values for $3\pi^0$. The lower resonance also moves down in mass very significantly.

In $3\pi^0$ data, the lower resonance $f_0(1335)$ is largely hidden beneath $f_2(1270)$ and its presence is revealed only by amplitude analysis. However, the dip between it and

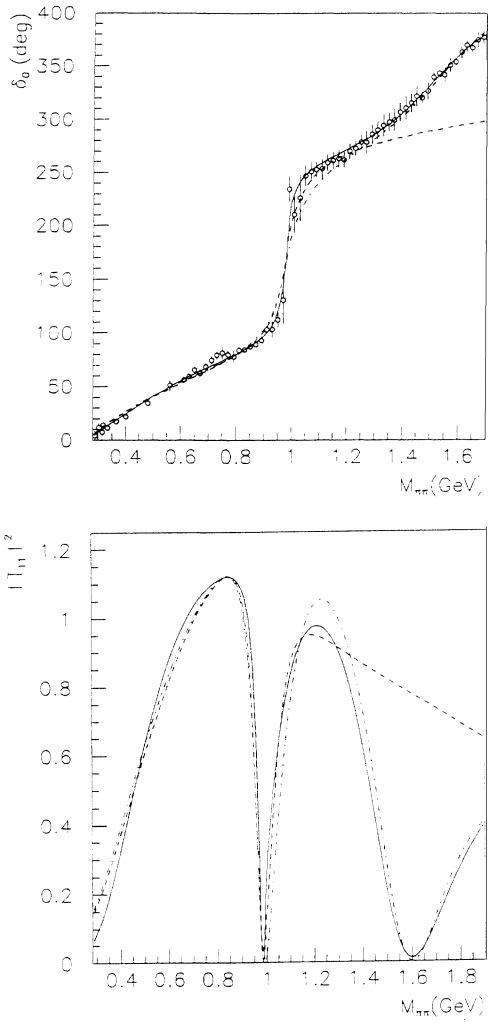

FIG. 14. The phase shift δ_S for S-wave $\pi\pi$ elastic scattering; the data are from Refs. [29–31]. Solid, dashed, and chain curves are our fits III, I, and II, (b) $|T_{11}|^2$, the $\pi\pi\to\pi\pi$ intensity from II.

$f_0(1505)$ is visible in the $3\pi^0$ data, just as in $\eta\eta\pi^0$ data. The precise mass dependence depends delicately on the exact parametrization of the amplitude, but in all fits comes out considerably lower than the 1430 MeV estimate given in Ref. [14]. It is visible to the naked eye that in Fig. 14 the lower f_0 band peaks in mass below 1430 MeV. With our parametrization of amplitudes, a fit to $\eta\eta\pi^0$ data alone puts the lower f_0 resonance at 1334 MeV with a width of 298 MeV.

A. The $\pi\pi\to\pi\pi$ S-wave amplitude

The essential point emerging from Sec. II is that the denominator function $D(s)$ should be identical for 0^{++} amplitudes in $\pi\pi\to\pi\pi$, $\pi\pi\to K\bar{K}$, $\bar{p}p\to 3\pi^0$, and $\bar{p}p\to\eta\eta\pi^0$. In order to constrain the fit as tightly as possible we fit all four data sets simultaneously with consistent parameters. We have ignored the $\pi\pi$ $I=2$ S wave, since it is almost constant and cannot be distinguished from a slowly varying component in the $I=0$ S wave.

We fit values of δ_S and η extracted from (a) K_{e4} data by Rosselet *et al.* [29], and from CERN-Munich data [30] by Ochs [31]. Data are shown in Fig. 14 with our fits, whose detailed forms are given below.

However, before going into detail we draw attention to a small but unavoidable conflict between Ochs' results and Crystal Barrel data above about $s=1.2$ GeV^2. The former gives a value of δ_S rising slowly and steadily and executing a slow loop on the Argand diagram. Most of our fits to Ochs' data give a pole at $M=1.5$ to 1.55 GeV with a large and poorly established width. The Particle Data Group [32] (PDG) quotes a mass of 1400 MeV and a width of 150 to 400 MeV. Au, Morgan, and Pennington [33] describe several fits with masses in the range 1360 to 1520 MeV and widths varying from 340 to 520 MeV data. However, the data on $\bar{p}p\to 3\pi^0$ require instead two narrow resonances centered around $M=1335$ and 1505 MeV, with a cusp between them at about 1430 MeV (Fig. 16 below). We suggest that the CERN-Munich data have not resolved these two resonances. This may have arisen because, in the CERN-Munich data, the S wave is obscured by the presence of strong F- and D-wave resonances and an uncertain P wave; the $\rho'(1600)$ of the 1970–1980 era has today split into the $\rho'(1465)$ and $\rho'(1700)$ of Donnachie and Clegg [34] and this will have some affect on the extracted S wave. It is also possible that these resonances couple strongly to 4π and show up weakly in $\pi\pi\to\pi\pi$. Figure 15 shows the difference between Ochs' fit to $\pi\pi\to\pi\pi$ and the best fit using our widths for $f_0(1335)$ and $f_0(1505)$; however, the latter ignores any background nonresonant contribution, which could complicate the situation. In fitting data we have to be careful to avoid "double counting" of the broad resonance in Ochs' results and the narrower resonances required by the $\bar{p}p$ data.

There is further evidence pointing toward two resonances rather than one. Central production data of

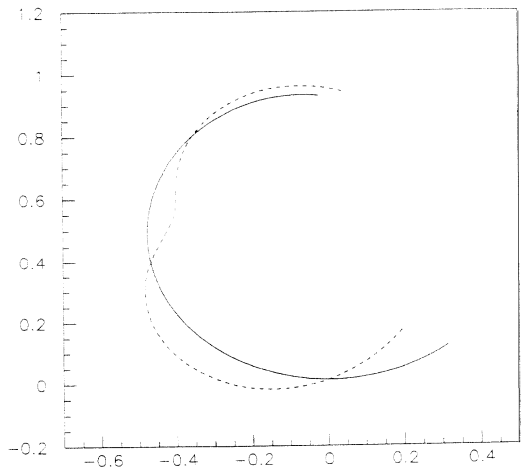

FIG. 15. The Argand diagrams for $\pi\pi\to\pi\pi$ amplitudes (a) fitting δ_S of Ochs [31] with a single broad resonance, (b) fitting with $f_0(1335)$ and $f_0(1505)$.

WA76 [35] have a shoulder at 1430 MeV, leading the group to claim a 0^{++} resonance with $M=1472\pm12$ MeV, $\Gamma=195\pm33$ MeV, superposed on a mass distribution falling rapidly with s. It seems likely that the shoulder at 1430 meV is the same phenomenon as the cusp we see at this energy.

We now discuss the algebraic forms we have adopted in fitting both $\pi\pi\to\pi\pi$ and annihilation data. Our strategy has been to try a variety of fits with different parametrizations of the S-wave amplitude, in order to establish the range of possible masses and widths for the two resonances and indeed to establish that two resonances are really required. We fit data at all energies with

$$f(\pi\pi\to\pi\pi)=T_{11}(s)=N(s)/D(s) \tag{29}$$

and

$$f_{\bar{p}p}=T'_{11}(s)+\frac{\Lambda_1}{s-M_1^2+iM_1\Gamma_1}+\frac{\Lambda_2}{s-M_2^2+iM_2\Gamma_2}+C\ , \tag{30}$$

where

$$T'_{11}(s)=N'(s)/D(s)\ , \tag{31}$$

and $\Lambda_{1,2}$ are complex coupling constants. That is, we superpose on the $\pi\pi$ amplitude two Breit-Wigner (BW) amplitudes which accommodate the new resonances demanded by the annihilation data. If these extra resonances are added to the $\pi\pi\to\pi\pi$ amplitude of Eq. (29), there is great latitude depending on what assumptions are made about coupling to 4π and a possible nonresonant background contribution. Note that the denominators of Eqs. (29) and (31) are identical functions $D(s)$, but the numerators $N(s)$ and $N'(s)$ are different.

In fitting $\bar{p}p$ data we have adopted two alternative strategies and fitted the data both ways. Both give similar results. In the first strategy we fit δ_S only up to $s=1.2$ GeV^2 and allow the $\pi\pi\to\pi\pi$ amplitude to be free above this energy. We fit $\bar{p}p$ data up to $s=1.2$ GeV^2 with Eq. (30). Then above $s=1.2$ GeV^2 we make a smooth join to

$$f_{\bar{p}p}=a+bs+cs^2+\frac{\Lambda_1}{s-M_1^2+iM_1\Gamma_1}+\frac{\Lambda_2}{s-M_2\Gamma_2+iM_2\Gamma_2}\ . \tag{32}$$

This explicitly avoids any possible double counting above $s=1.2$ GeV^2. The term $a+bs+cs^2$ contains no poles, so there is no ambiguity in identifying the leading singularities. In principle, there is the disadvantage of a nonanalytic change of slope at $s=1.2$ GeV^2, but in practice the eye can barely discern it on most of our Argand diagrams. In the parabolic background, a, b, and c are complex parameters.

In the second strategy, δ_S has been fitted up to 1.8 GeV with forms II and III given below and $\bar{p}p$ data have been fitted with Eq. (30). If our parametrization describes the Dalitz plot well, we can consider the Argand plot as some kind of new experimental data and fit these data by BW resonances and a background term. We have found that the characteristics of the BW resonances extracted like this are stable, while the remaining amplitude including the pole in T_{11} and T'_{11} can be approximated very closely by a parabolic background. This demonstrates that the distant pole in CERN-Munich data near 1550 MeV plays a rather insignificant role in the fit to $\bar{p}p$ data and the determination of the BW resonances in the latter.

We now come to the three explicit forms we have fitted to $\pi\pi\to\pi\pi$ and $\pi\pi\to K\bar{K}$. In the two channel case, the denominator $D(s)$ has only right-hand singularities connected with $\pi\pi$ and $K\bar{K}$ production, and therefore can be written generally in the form

$$D(s)=g_0(s)-i\rho_1 g_1(s)-i\rho_2 g_2(s)-\rho_1\rho_2 g_3(s)\ . \tag{33}$$

This denominator can be rewritten in the K-matrix form by the substitution

$$K_{11}=\frac{g_1(s)}{g_0(s)},\quad K_{23}=\frac{g_2(s)}{g_0(s)}\ ,$$
$$K_{12}=K_{21}=\frac{\sqrt{g_1(s)g_2(s)-g_0(s)g_3(s)}}{g_0(s)}\ . \tag{34}$$

With the relation between T matrix and K matrix,

$$T=\frac{1}{1-\rho_1\rho_2 D_K-i(\rho_1 K_{11}+\rho_2 K_{22})}\begin{bmatrix}K_{11}-i\rho_2 D_K & K_{12}\\ K_{21} & K_{22}-i\rho_1 D_K\end{bmatrix}\ , \tag{35}$$

where D_K is the determinant

$$D_K=K_{11}K_{22}-K_{12}^2\ , \tag{36}$$

we have the $\pi\pi$ scattering amplitude as

$$T=\frac{1}{D(s)}\begin{bmatrix}g_1(s)-i\rho_2 g_3(s) & \sqrt{g_1(s)g_2(s)-g_0(s)g_3(s)}\\ \sqrt{g_1(s)g_2(s)-g_0(s)g_3(s)} & g_2(s)-i\rho_1 g_3(s)\end{bmatrix}\ . \tag{37}$$

In our first approach, labeled I, we have used a simple two-pole parametrization of functions $g_i(s)$:

$$g_0(s)=(s-s_1)(s-s_2)\ , \tag{38}$$

$$g_1(s)=\gamma_1+\gamma_2 s\ , \tag{39}$$

$$g_2(s)=\gamma_3+\gamma_4 s\ , \tag{40}$$

$$g_3(s)=\gamma_5+\gamma_6 s\ , \tag{41}$$

$$\rho_1(s)=[(s-4m_\pi^2)/s]^{1/2}\ , \tag{42}$$

$$\rho_2(s)=\begin{cases}[(s-4m_K^2)/s]^{1/2} & \text{for } s>4m_K^2\ , \\ +i[(4m_K^2-s)/s]^{1/2} & \text{for } s<4m_K^2\ .\end{cases} \tag{43, 44}$$

We take an average $M_K=0.495\,67$ GeV and the best fit gives (in units of GeV)

$$s_1=0.155,\quad s_2=1.536,\quad \gamma_1=3.545\ ,$$

$$\gamma_2=-3.728,\quad \gamma_3=1.765,\quad \gamma_4=-1.291\ ,$$

$$\gamma_5=-0.433,\quad \gamma_6=1.134\ .$$

This form fits the $\pi\pi\to\pi\pi$ data well only up to $M_{\pi\pi}=1.3$ GeV (see Fig. 14). Above this mass, the additional poles due to $f_0(1335)$ and $f_0(1515)$ fit the annihilation data.

In our second approach, labeled II, we have parametrized in a three-pole form the elements of the K matrix:

$$K_{ij}=\left(\frac{s-2m_\pi^2}{s}\right)\left(\frac{\alpha_i\alpha_j}{s_A-s}+\frac{\beta_i\beta_j}{s_B-s}+\frac{\gamma_i\gamma_j}{s_C-s}+A_{ij}+B_{ij}s\right)\ . \tag{45}$$

We obtain the parameters (in GeV)

$$s_A=0.7239,\quad s_B=1.5279,\quad s_C=3.9657\ ,$$

$$\alpha_1=0.6941,\quad \alpha_2=0,\quad \beta_1=0.8974\ ,$$

$$\beta_2=0.0049,\quad \gamma_1=1.6385,\quad \gamma_2=-2.1499\ ,$$

$$A_{11}=-0.2905,\quad A_{12}=2.0219\ ,$$

$$A_{22}=-0.4376,\quad B_{11}=-0.2049\ ,$$

$$B_{12}=0,\quad B_{22}=0\ .$$

These two parametrizations I and II are different in the following point: in the first we use a simple parametrization of the function $D_K=K_{11}K_{22}-K_{12}^2$ and thus a complicated expression for K_{12}; in the second we use a simple expression for K_{12} while the D_K function has a complicated structure. Both forms give a very close description of $\pi\pi$ scattering up to 1.1 GeV; the third pole of form II is required to fit CERN-Munich data in the 1300–1700 MeV mass range.

The third form we have used, labeled III, is based on the Dalitz-Tuan representation [36]:

$$T_{11}=\frac{e^{2i\phi}-1}{2i\rho_1}+\frac{g_1 e^{2i\phi}}{M_R^2-s-i(\rho_1 g_1+\rho_2 g_2)}\ , \tag{46}$$

$$T_{12}=\frac{\sqrt{g_1 g_2}\,e^{i\phi}}{M_R^2-s-i(\rho_1 g_1+\rho_2 g_2)}\ , \tag{47}$$

$$T_{22}=\frac{g_2}{M_R^2-s-i(\rho_1 g_1+\rho_2 g_2)}\ , \tag{48}$$

$$e^{2i\phi}=\frac{1+a_1 s+a_2 s^2+i\rho_1[b_1(s-m_\pi^2/s)+b_2 s^2]}{1+a_1 s+a_2 s^2-i\rho_1[b_1(s-m_\pi^2/s)+b_2 s^2]}\ . \tag{49}$$

Numerical values of parameters, in units of GeV, are

$$M_R=0.9535,\quad g_1=0.1108,\quad g_2=0.4229\ ,$$

$$a_1=-0.3835,\quad a_2=-0.4237\ ,$$

$$b_1=3.696,\quad b_2=-1.462\ .$$

The last two of these parametrizations were investigated by Zou and Bugg [37]. They have a pole in the T'_{11} term of Eq. (30) in the region of 1400–1500 MeV, i.e., the region of our BW resonances $f_0(1335)$ and $f_0(1505)$. In practice, we have found this not to be a significant problem, since the $\bar{p}p$ data identify the contributions from the nearby BW poles cleanly.

Table I summarizes the second and third sheet poles present in forms I, II, and III. The second sheet is defined by

$$\mathrm{Im}\rho_1(s)<0,\quad \mathrm{Im}\rho_2(s)>0\ , \tag{50}$$

and the third by

$$\mathrm{Im}\rho_1(s)<0,\quad \mathrm{Im}\rho_2(s)<0\ . \tag{51}$$

As a final comment on the complexity of this mass range we remark that the 4π inelastic threshold opens strongly from $M=1$ to 1.6 GeV, presumably because of $\sigma\sigma$ and $\rho\rho$ thresholds. The data of Alston-Garnjost *et al.* [38] on $\pi\pi\to\pi\pi$, $K\bar{K}$, and 4π can be fitted crudely by a Fermi function

$$\Gamma_{4\pi}=\frac{\Lambda_{4\pi}}{1+\exp[(s_0-s)/a_0]} \tag{52}$$

with $s_0=1.44$ GeV^2 and $a_0=0.25$ GeV^2. In some fits we have tried accommodating the 4π channel by Breit-Wigner amplitudes of the form

$$X_{\mathrm{BW}4\pi}=\frac{\Lambda}{s-M^2+iM(\Gamma_{2\pi}+\Gamma_{4\pi})}\ . \tag{53}$$

TABLE I. Second and third sheet poles present in forms I–III, in GeV.

Form	Sheet II	Sheet III
I	$0.984-0.039i$	$0.986-0.102i$
II	$0.987-0.053i$	$0.954-0.060i$ $1.071-0.290i$ $1.548-0.183i$
III	$0.98-0.023i$	$0.797-0.185i$ $0.408-0.342i$ $1.515-0.214i$

Although this form modifies parameters $N'(s)$ and $a+bs+cs^2$ in Eqs. (31) and (32), there is no significant improvement in fits. The data are presently not adequate to attempt a 3-channel fit to $\pi\pi$, $K\bar{K}$, and 4π, let alone a 4-channel fit to $\pi\pi$, $K\bar{K}$, $\rho\rho$, and $\sigma\sigma$.

B. Fits to $\bar{p}p \to 3\pi^0$ and $\bar{p}p \to \eta\eta\pi^0$

In order to give some feeling for the stability of resonance parameters, we shall present several fits to the data. All assume annihilation from a pure $^1S_0$ initial state. In Sec. III E we report studies including P-state annihilation. These studies show that the fraction of P-state annihilation is $<10\%$ and has little impact on the results presented now.

With the assumption of S-state annihilation, the initial state is restricted by G parity to $I=1$ $^1S_0$. Annihilation from the $^3S_1$ initial state is forbidden. In the final state, 0^{++} $\pi\pi$ and $\eta\eta$ states are produced with $L=0$ and 2^{++} states with $L=2$. For the latter we include $f_2(1270)$ and $f_2'(1525)$ with masses and widths fixed to PDG values.

In $\eta\pi$ we include $a_0(980)$, fitted to a Flatté form:

$$A(980)=\frac{\Lambda_{980}}{s-M_{980}^2+iM_{980}(g_1\rho_1+g_2\rho_2)}\ , \tag{54}$$

where

$$\rho_1=[s-(M_\pi+M_\eta)^2]^{1/2}[s-(M_\pi-M_\eta)^2]^{1/2}/s \tag{55}$$

and ρ_2 is given by Eqs. (43) and (44). We adjust parameters of the Flatté form in order to reproduce as closely as possible the parameters of the Breit-Wigner amplitude of the Particle Data Group, but with the ratio g_2/g_1 fixed to the mean value of Lockman [39]. We find a negligible contribution to $\eta\eta\pi$ data from $a_2(1320)$. In fitting $3\pi^0$ data we find it necessary to add a further D-wave contribution above $f_2(1270)$ at a mass of about 1560 MeV. This important detail will be discussed at some length in a latter subsection.

For $L=2$, $J=2$, we include a centrifugal barrier factor for both production and decay. The contribution to the scattering amplitude is

$$T(s)=\frac{\Lambda(B_2/B_{2R})}{s-M_R^2+iM_R\Gamma}\ . \tag{56}$$

The nonrelativistic form for B_2 is

$$B_2=\frac{|\mathbf{k}_3|^2|\mathbf{k}_1|^2(3\cos^2\theta-1)/2}{[|\mathbf{k}_3|^2(|\mathbf{k}_3|^2+X_2)+X_2^2]^{1/2}[|\mathbf{k}_1|^2(|\mathbf{k}_1|^2+X_2)+X_2^2]^{1/2}}\ , \tag{57}$$

where $\mathbf{k}_3$ is the momentum of the spectator in the laboratory system, $\mathbf{k}_1$ is the momentum of decay products of the resonance in the rest frame of the resonance, and θ is the decay angle; B_{2R} is the value of B_2 on resonance for $\cos\theta=1$. The value of X_2 is optimized to a value $X_2=0.356$ GeV, corresponding to a range of interaction of 0.6 fm.

The relativistic version of the centrifugal barrier is (omitting the Hippel-Quigg form factor temporarily)

$$B_2=[k_{12\mu}^{\perp}k_{12\nu}^{\perp}-\tfrac{1}{3}g_{\mu\nu}^{\perp}(k_{12}^{\perp})^2][k_{3\mu}^{\perp}k_{3\nu}^{\perp}-\tfrac{1}{3}\tilde{g}_{\mu\nu}^{\perp}(k_3^{\perp})^2]\ ,$$

where

$$g_{\mu\nu}^{\perp}=g_{\mu\nu}-(k_1+k_2)_\mu(k_1+k_2)_\nu/(k_1+k_2)^2\ ,$$

$$\tilde{g}_{\mu\nu}^{\perp}=g_{\mu\nu}-P_\mu P_\nu/P^2\ ,$$

$$P_\mu=(k_1+k_2+k_3)_\mu\ ,$$

$$k_{12\mu}^{\perp}=(k_1-k_2)_\nu g_{\nu\mu}^{\perp},\quad k_{3\mu}^{\perp}=k_{3\nu}\tilde{g}_{\nu\mu}^{\perp}\ .$$

This result differs from the nonrelativistic one by a factor Y in the numerator with

$$Y=\frac{4}{9}\left[\frac{(W^2-M_3^2+s_{12})^2}{s_{12}W^2}+2\right]\ , \tag{58}$$

where W is the total $\bar{p}p$ center of mass energy, M_3 is the mass of the spectator meson, and s_{12} is the mass squared of the resonance.

In fitting the S-wave amplitudes, it is necessary to include considerable flexibility in the numerator $N'(s)$ of Eq. (31), in order to accommodate the complicated dynamics of Figs. 10 and 12. In $3\pi^0$ data demand a large S-wave amplitude close to threshold and also at large s, with a small amplitude in between, around the hole in the middle of the Dalitz plot. Figure 16(a) shows the Argand diagram for our eventual recommended fit, which is the best compromise among fitted masses and widths for resonances. There is a broad loop at low energies corresponding to the σ peak at 800 meV. This is followed by a small loop due to $f_0(975)$. Near this mass, the amplitude squared reaches a minimum. Then follow loops due to resonances at 1335 and 1505 MeV, with a second minimum of the amplitude squared between them at 1430 MeV.

In order to show the effect of the Λ parameters which scale the $\pi\pi$ amplitude in fitting annihilation data, Fig. 17 displays $|N(s')|/|N(s)|$ for $3\pi^0$. This is the ratio of the annihilation amplitude in the $\pi\pi$ S wave to that for elastic scattering. It displays nicely the peak-dip structure of the Bettini *et al.* data as a function of s.

With form I we take for $N'(s)$ the parametrization

$$N'(s)=\Lambda_1+\Lambda_2 s-i\rho_2(\Lambda_3+\Lambda_4 s)\ . \tag{59}$$

The term involving ρ_2 allows coupling via intermediate $K\bar{K}$ channels. We have found empirically that fits with less Λ parameters give significantly poorer χ^2 and sys-

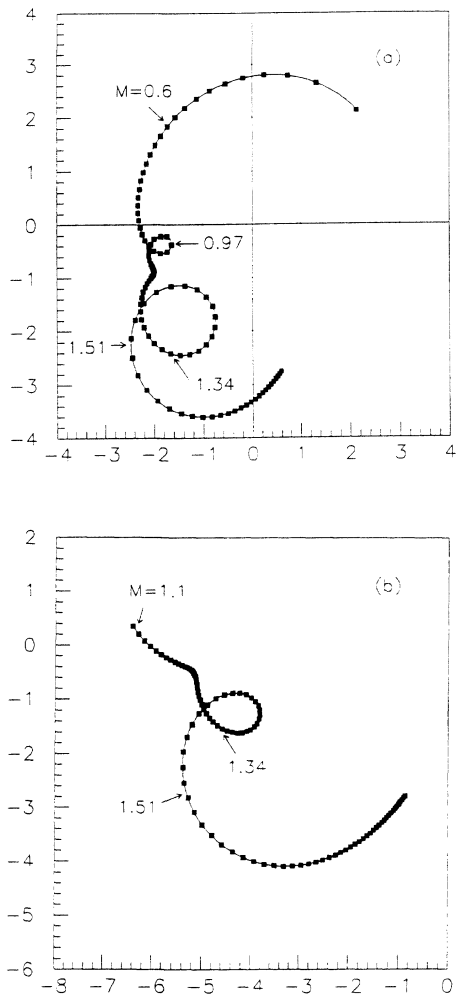

FIG. 16. Argand diagrams for (a) the $\pi\pi$ S-wave amplitude fitted to $\bar{p}p \to 3\pi^0$, from our "best" fit, (b) the $\eta\eta$ S-wave amplitude fitted to $\bar{p}p \to \eta\eta\pi^0$.

tematic discrepancies with data. Form (59) marginally underfits the data, in the sense that all peaks and dips in the data are very slightly smoothed out in the fit. The most complicated form we have tried with the forms II and III is

$$N'(s)=\left[\Lambda_1+\Lambda_2 s+\frac{\Lambda_3}{s-s_0}\right]T_{11}+(\Lambda_4+\Lambda_5 s)T_{12}\ . \tag{60}$$

The coefficient of T_{11} allows in a natural way the $\pi\pi$ S-wave amplitude to be large at low s, small around $s=1$ GeV^2, and large again for large s. The term $\Lambda_3/(s-s_0)$ allows the possibility of canceling the Adler zero, which need not be present in coupling of $\pi\pi$ to $\bar{p}p$. Although Eq. (60) gives the very best χ^2, its flexibility is such that convergence is poor. The reason is that the term $(\Lambda_4+\Lambda_5 s)T_{12}$, which accommodates coupling through intermediate $K\bar{K}$ states, correlates strongly with Λ_2 and Λ_3.

We have found empirically that an alternative numerator, giving almost as good χ^2 and much more rapid convergence is

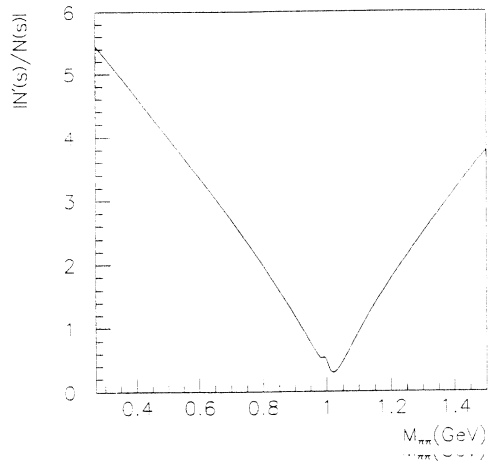

FIG. 17. $|N'(s)|/|N(s)|$ for the fit of Table III to the $\pi\pi$ S wave in $\bar{p}p \to 3\pi^0$.

$$N'(s)=(\Lambda_1+\Lambda_2 s)K_{11}+i\rho_2(\Lambda_3+\Lambda_4 s)(K_{11}K_{22}-K_{12}^2) \tag{61}$$

with form II. Many of the results we shall show are obtained with this form because of its rapid convergence.

With form III, we multiply the term $(e^{2i\phi}-1)/2i\rho_1$ of Eq. (46) by $\Lambda_1+\Lambda_2 s$, the resonance term in (46) by Λ_3, and T_{12} by Λ_4. In our second strategy, where the N/D term is cut off above $s=1.2$ GeV^2, we take $N'(s)=\Lambda_1+\Lambda_2 s$, because of the limited mass range.

We have investigated systematically permutations of (a) forms I to III for the $\pi\pi$ S wave, (b) whether or not the cut-off at $s=1.2$ GeV^2 is applied, (c) with or without $\Gamma_{4\pi}$ in $f_0(1335)$ and $f_0(1505)$, (d) nonrelativistic or relativistic centrifugal barriers. Several hundred different fits have been made with these and other variants described later. A representative sample of Argand diagrams is shown in Figs. 18 and 19 for the $\pi\pi$ S-wave amplitude in $\bar{p}p \to 3\pi^0$. Corresponding resonance parameters and χ^2 are listed in Table II. Differences between nonrelativistic centrifugal barriers or relativistic have little effect on resonance parameters.

The mass and width of $f_0(1505)$ are very stable. The mass of $f_0(1335)$ is rather less stable, because the resonance is broader, making the maximum of its speed plot harder to determine, and also because the resonance lies under $f_2(1270)$ and is revealed by interference with it. The absolute extremes we have observed for the mass of $f_0(1335)$ are 1295 and 1395 MeV. However, all those outside the range 1306 to 1365 MeV have features (e.g., poor convergence) which indicate poor numerical stability. We regard the latter range as the maximum plausible for the mass of the resonance and add 10 MeV for statistical fluctuations, making the limits of error on the mass ± 40 MeV. From Table II the maximum range of widths is 218 to 330 MeV. We therefore assess the error on the width of $f_0(1335)$ as ± 45 MeV. In our final compromise fit, given in Table III and using form IIP for the $\pi\pi$ S wave, we fix the masses and widths of the two resonances at the central values from Table II. This of course does

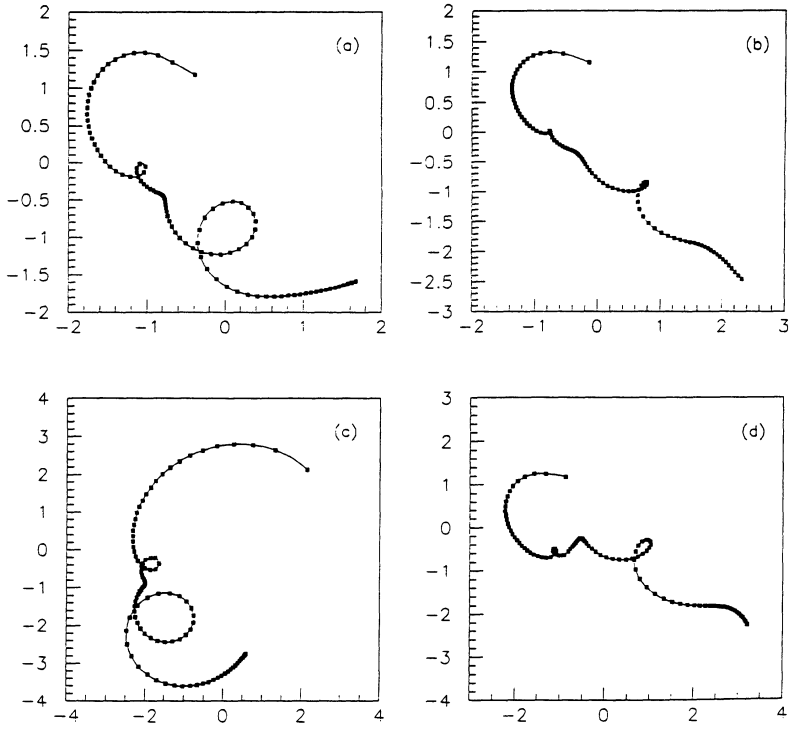

FIG. 18. Argand diagrams (a)–(d) for the $\pi\pi$ S-wave amplitude in $\bar{p}p \to 3\pi^0$ for lines 1–4 of Table II.

not give quite the optimum χ^2, but is close.

Fits with $N'(s)/D(s)$ cut off at $s=1.2$ GeV^2 tend to give lower masses for $f_0(1335)$ and $f_0(1505)$ than those where $N'(s)/D(s)$ is used for all energies. On the other hand, a feature favoring higher masses is that those fits where these resonances include $\Gamma_{4\pi}$ of Eq. (52) give masses systematically higher by about 25 MeV for $f_0(1335)$ and by about 7 MeV for $f_0(1505)$.

There can be no doubt that the data require both $f_0(1335)$ and $f_0(1505)$. As reported in Ref. [16], χ^2 increases by a factor 5 for $3\pi^0$ data if $f_0(1505)$ is replaced by a 2^+ resonance, and χ^2 doubles for $\eta\eta\pi^0$ data. If the two resonances are reduced to one, χ^2 rises from 720 to 1377, with $M=1472$ MeV, $\Gamma=136$ MeV. The mass of $f_0(1505)$ is better defined by $3\pi^0$ data, but a fit to $\eta\eta\pi^0$ alone gives $M=1512$ MeV, $\Gamma=158$ MeV. The mass of

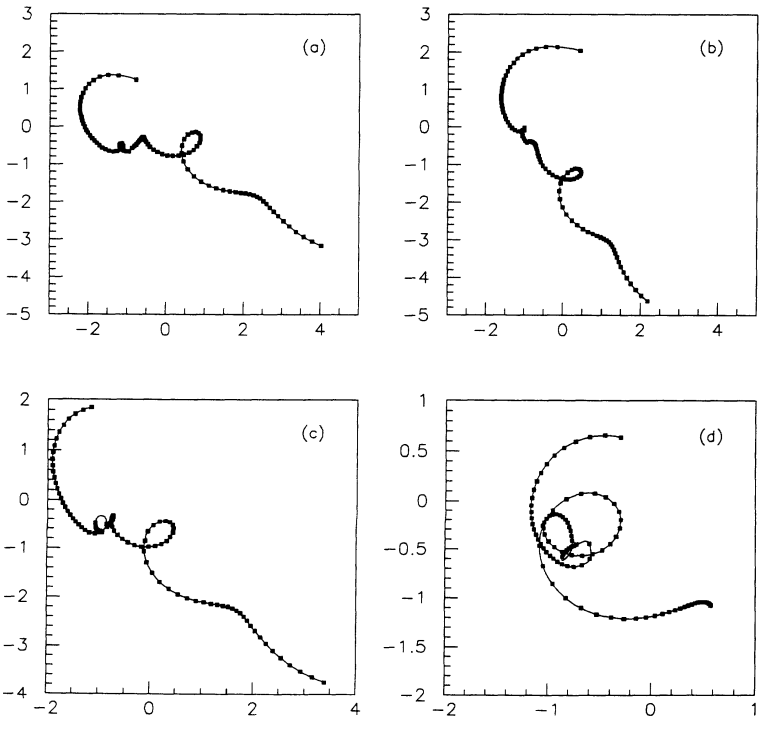

FIG. 19. Argand diagrams (a)–(d) for the $\pi\pi$ S-wave amplitude in $\bar{p}p \to 3\pi^0$ for lines 5–8 of Table II.

TABLE II. A variety of fits to $3\pi^0$ and $\eta\eta\pi^0$ data. Resonance masses and widths are given in MeV. In the first three fits, the $\pi\pi$ S-wave amplitude of Eq. (31) is used for all s. In the remainder, this form is used below $s=1.2$ GeV^2 and above this is replaced by either (i) P, a parabolic form, Eq. (32) without $\theta(1710)$, or (ii) L, a linear form $a+bs$, plus $\theta(1710)$ with mass and width taken from the PDG. All fits use a nonrelativistic centrifugal barrier, except those marked with an asterisk, indicating a relativistic barrier.

	Form of $\pi\pi$ S wave	Λ used	M_1	Γ_1	M_2	Γ_2	M_D	Γ_D	χ^2
1	II	1–4	1365	268	1520	148	1566	169	720
2	II*	1–4	1360	330	1512	170	1552	168	726
3	I*	1–4	1317	250	1497	143	1558	163	798
4	II,P	1,2	1328	242	1500	142	1560	179	795
5	II,L	1,2	1312	258	1498	158	1568	189	888
6	II,P	1–3	1324	260	1509	159	1560	173	740
7	III,L	1,2,4	1310	259	1495	160	1570	190	820
8	III,P	1,2	1319	218	1499	136	1573	174	781

$f_0(1335)$ is defined rather better by $3\pi^0$ data, but its width is equally sensitive to $3\pi^0$ and $\eta\eta\pi^0$ data. A fit to $\eta\eta\pi^0$ data alone gives $M=1334$ MeV, $\Gamma=298$ MeV for the lower f_0 resonance.

In all fits where $N'(s)/D(s)$ is cut off at $s=1.2$ GeV^2, the parabolic term in $a+bs+cs^2$ is negative. It is therefore not simulating $f_0(1335)$ or $f_0(1505)$. Instead, the trends of the Argand plots of Figs. 17 and 18 at the highest s show that it is suggesting the onset of yet another resonance at a mass close to the end of phase space. The quark model leads us to expect a radial excitation around a mass of 1700–1800 MeV. There is indeed controversial evidence that $\theta(1710)$ has $J^P=0^+$ [40], although the WA76 Group [41] maintains with high statistics data a claim for $J^P=2^+$. In several fits we have introduced $f_0(1710)$ with fixed mass, and with width Γ either equal to the value 148 MeV of the PDG or varying freely. The fits definitely prefer $\Gamma\simeq 250$–300 MeV. However, from a conservative point of view, the data do not show any bump positively suggesting a resonance of this mass. Therefore we do not claim the existence of this resonance, but simply that the data would accommodate naturally to its existence.

C. $G(1590)$

The GAMS Group has presented extensive evidence for a 0^{++} resonance in $\eta\eta$ and $\eta\eta'$ at 1590 MeV [42]. We have tried including it with PDG values in fits to both $3\pi^0$ and $\eta\eta\pi^0$ data. Of course, χ^2 improves, but rather marginally. For $\eta\eta\pi^0$, the improvement in χ^2 is 11.8, which is not really significant compared with changes obtained by varying the form of $N'(s)$. If $f_0(1505)$ is omitted and replaced by $G(1590)$ with PDG values, χ^2 for $\eta\eta\pi^0$ rises from typically 370 to 482. If the mass is fixed at 1587 MeV and the width is varied, χ^2 decreases only by 1 and $\Gamma\rightarrow 188$ MeV. In summary, the Crystal Barrel data show no real positive evidence for $G(1590)$. It might not couple strongly to $\bar{p}p$ if it is dominantly an $s\bar{s}$ state.

D. The $\pi\pi$ D-wave amplitude

Here we have a puzzle which is not fully resolvable with present data. The fit to $\bar{p}p\rightarrow 3\pi^0$ data definitely demands a contribution to the $\pi\pi$ D wave at a mass of ~ 1560 MeV. Without it, χ^2 increases by about a factor 1.5. Although this is a highly significant increase in χ^2, it is much less than that due to $f_0(1505)$. We have parametrized the D-wave contribution at 1560 MeV in Tables II and III as a simple Breit-Wigner resonance. The fitted mass and width are stable in Table II, but this reflects to some extent the fact that the parameter X_2 of the centrifugal barrier is fixed there. The presence of the extra D wave is demanded by data at the very edge of the Dalitz plot, near $\cos\theta=\pm 1$, rather than by the bump B of

TABLE III. Our compromise fit with masses of the two f_0 resonances taken at central values of Table II, using form II for the $\pi\pi$ S wave for $s<1.2$ GeV^2 and Eq. (32) for $s>1.2$ GeV^2.

Amplitude	M	$(\Gamma\rho)_{\rm res}$	Λ
$f_0(1335)$	1.335	0.260	$0.611-i0.493$
$f_0(1505)$	1.505	0.150	$-0.077-i0.695$
$f_2(1270)$	1.275	0.205	1.0
f_D	1.555	0.179	$0.519+i0.614$
$\pi\pi$ S wave	$\Lambda_1=-1.249+i6.153$	$\Lambda_2=-1.181-i5.757$	$C=-0.899-i0.895$
	$\Lambda_3=0.0$	$\Lambda_4=0.0$	
	$a=-6.919-i8.956$	$6.676+i8.935$	$-0.888-i2.225$

Fig. 10 near $\cos\theta=0$. The Argand diagram of the $\pi\pi$ D wave is shown on Fig. 20.

One must be cautious about interpreting this as evidence for a new resonance, although there have been several claims from DESY [43] for large amplitudes for $\gamma\gamma\to\rho\rho$, possibly resonant. The $L=2$ centrifugal barrier plays a strong role at this mass. If there is any contribution from higher resonances, they will be attenuated strongly at the top of phase space, so the narrow width of the D-wave state may reflect the effect of the centrifugal barrier. There are resonances listed by the PDG with masses of 1430, 1515, 1640, and 1810 MeV, not to mention $f_2'(1525)$ (which decays overwhelmingly to $K\bar{K}$) and the possibility of $\theta(1710)$ with $J=2$. Some combination of these can mock up our D-wave contribution.

It has been drawn to our attention by Ochs [44] that CERN-Munich data [45] also show evidence for a minimum at about 1460 MeV in moments Y_1^0, Y_2^0, Y_3^0, and Y_4^0, so it seems likely to be a real physical effect in the D wave, whatever its explanation. In $\bar{p}p$ data, it seems to be associated with a line of zeros of Fig. 13 propagating through the edge of the Dalitz plot, and forming the cusp of Fig. 20 at 1430 MeV.

We have tried several modifications to the D-wave contribution above $f_2(1270)$. Firstly, in order to study the effect of the $\rho\rho$ threshold, we have given the $f_2(1270)$ a width for decay of the form of Eq. (52), and normalized its strength to the PDG branching ratio of 6.9% on resonance. This produces only a tiny change in χ^2 of 1 and does nothing to eliminate the need for a contribution centered at 1560 MeV. The implication is that, if the $\rho\rho$ threshold plays a role, rescattering back to the 2π channel modifies $\Gamma_{2\pi}$ in such a way as to generate the cusp at 1430 MeV.

Secondly, Vandermeulen [46] has pointed out that high mass states are enhanced. This is probably a form factor effect: high mass states are produced with a small momentum transfer, q. Figure 20 suggests that the high mass side of the $f_2(1270)$ may be enhanced by this effect. We have tried including the Vandermuelen factor explicitly into the fit. It helps slightly in reducing χ^2 and the D-state contribution at 1560 MeV, but does not eliminate it.

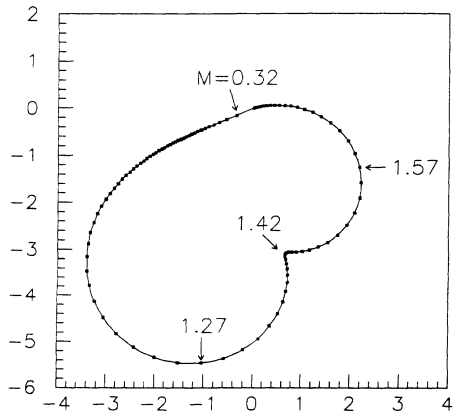

FIG. 20. The Argand diagram for the $\pi\pi$ D wave.

In summary, we find the D-state contribution above $f_2(1270)$ to be indispensable and similar to that observed in the CERN-Munich experiment; but we are not confident of its precise explanation. It is risky at present to interpret it as definitive evidence for a new resonance, because of the restricted phase space and centrifugal barrier. Its statistical significance is a factor 10 less than $f_0(1505)$ and its contribution to the cross section is less by a factor 7. A conservative explanation would be a combination of the $\rho\rho$ threshold and a $\bar{q}q$ resonance which is expected around 1700 meV.

E. *P*-state annihilation

The $A_X(1515)$ was originally claimed on the basis of Asterix data. It is therefore necessary that we confront our fits with these data. Our essential conclusion is that the Asterix data can be fitted well with $f_0(1515)$. The ambiguity arises because of (i) the large number of P-state annihilation amplitudes, listed below, (ii) the complexity of the $\pi\pi$ S wave as a function of $M_{\pi\pi}$. Asterix data alone are not conclusive in sorting out this very complicated story.

We first recapitulate the facts from the papers of the Asterix group. They measured P-state annihilation to $\pi^+\pi^-\pi^0$ in gaseous hydrogen, using an x-ray coincidence to identify a transition to the $2P$ state [47]. These data show a strong $A_X(1515)$ peak in $M(\pi^+\pi^-)$. In S-state annihilation in liquid hydrogen, the 1515 MeV peak is much smaller. The Asterix Group also made measurements in gaseous hydrogen without the x-ray coincidence [48]. Results lay midway between those from liquid and from pure P-state annihilation, and were compatible with the expected 50:50 mixture of P-state and S-state annihilation in gas at 1 atmosphere. The inference is that P-state annihilation favors production of $A_X(1515)$ and suggests $J^P=2^+$, because this would be strongly suppressed in S-state annihilation by the centrifugal barrier.

The snag with this argument is that S-state annihilation to $\pi^+\pi^-\pi^0$ is overwhelmingly dominated by the initial $^3S_1$ state $\to\rho\pi$, which makes up 85% of the cross section; $^3S_1$ annihilation to a final state involving $\pi\pi$ with $J=0$ or 2 is forbidden by C parity. The possibility remains that the much weaker (15%) $^1S_0$ annihilation may also lead to an A_X peak, and this is how we have interpreted the $3\pi^0$ data, to which $^3S_1$ annihilation does not contribute.

In fitting P-state annihilation, the Asterix Group tried assignments $J^P=0^+$ or 2^+ for $A_X(1515)$ and obtained a slightly better χ^2 with the latter hypothesis. A complication in the analysis is that the location of the A_X peak in, say, the s channel coincides closely with the crossing of two $\rho(770)$ bands in t and u channels. The Asterix Group argued that the A_X peak could not originate from a triple interference between the two $\rho(770)$ bands and A_X having $J^P=0^+$. This is the essential point where we differ. We use a more complicated form for the $\pi\pi$ S wave, which allows a good fit showing strong constructive interference. By discarding this interference, Asterix were pushed toward a 2^+ assignment for A_X, in order to explain the peak in the data near $\cos\theta=0$ in A_X decays.

We have fitted the Asterix data with x-ray coincidence [47] after applying a correction for the 8% of S-state annihilation, using data from Ref. [48]. These data correspond to pure initial P states. Masses and widths of resonances are fixed at values from Table III, and we use for $\rho'(1465)$ the parameters of Donnachie and Clegg [34]. The ingredients of the fit are

$$^3P_2 \to f_2(1270)\pi, \quad L=1 , \tag{62}$$

$$^3P_1 \to f_2(1270)\pi, \quad L=1 , \tag{63}$$

$$^3P_1 \to f_0(1505)\pi, \quad L=1 , \tag{64}$$

$$^3P_1 \to f_0(1335)\pi, \quad L=1 , \tag{65}$$

$$^3P_1 \to (\pi\pi)_S\pi, \quad L=1 , \tag{66}$$

$$^3P_2 \to \rho(770)\pi, \quad L=2 , \tag{67}$$

$$^3P_1 \to \rho(770)\pi, \quad L=0,2 , \tag{68}$$

$$^3P_1 \to \rho'(1465)\pi, \quad L=0 , \tag{69}$$

$$^1P_1 \to \rho(770)\pi, \quad L=0 , \tag{70}$$

$$^1P_1 \to \rho'(1465)\pi, \quad L=0 . \tag{71}$$

The Asterix Group included phase space amplitudes for final states. We have dropped these, but substituted the $\pi\pi$ S wave in the form of Eq. (30). We have used the form IIP for $(\pi\pi)_S$ given in Table III, but have multiplied it by a factor $(\Lambda_1+\Lambda_2 s)$ in order to allow for the fact that initial P states may couple to the $\pi\pi$ S wave with different coupling constants at different masses. In order to test the J^P assignment we have tried substituting $^3P_2$ and $^3P_1 \to A_X(1515)\pi$ with $L=1$ in place of $^3P_1 \to f_0(1505)\pi$.

Our fit differs from the Asterix Group by including a substantial amplitude for $^3P_1 \to (\pi\pi)_S\pi$, see Table IV. The phase variation of the $\pi\pi$ S wave plays a rather important role in the fit. The Argand diagram for our $(\pi\pi)_S$ amplitude is shown in Fig. 21. The $f_0(1505)$ amplitude is stronger than in S-state annihilation, Fig. 16.

The Asterix data alone do not give a strong differentiation between $J=0$ and $J=2$ for the resonance at 1505 or 1515 MeV. With $J=0$, $\chi^2=327$ and for $J=2$, $\chi^2=304$ for 231 degrees of freedom. The Asterix Group have only limited Monte Carlo statistics for their evaluation of acceptance, and in our quoted χ^2 we allow for statistical errors in this acceptance. We remark that the $J=2$ hypothesis allows two initial states, $^3P_2$ and $^3P_1$, giving different $\cos\theta$ dependence [47]; these two amplitudes give more freedom in the fit than the $J=0$ hypothesis, so the difference in χ^2 between these two hypotheses is not decisive.

TABLE IV. Fit to the Asterix x-ray data.

Initial state	Amplitude	Intensity (%)
$^3P_2$	$f_2(1270)\pi$	10.8
$^3P_1$	$f_2(1270)\pi$	11.7
$^3P_2$	$\rho(770)\pi, L=2$	9.5
$^3P_1$	$\rho(770)\pi, L=2$	8.1
$^3P_1$	$\rho(770)\pi, L=0$	3.3
$^3P_1$	$(\pi\pi)_S\pi$	18.6
$^1P_1$	$\rho(770)\pi, L=0+2$	36.9
$^3P_1$	$\rho'(1465)\pi, L=0$	1.1

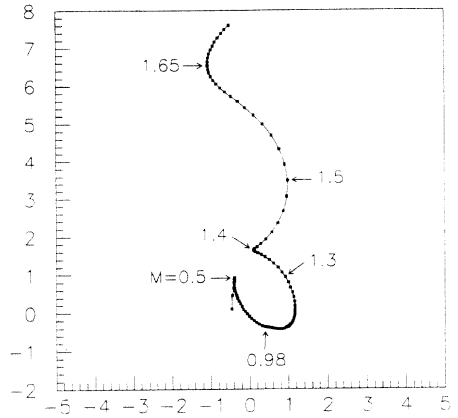

FIG. 21. The Argand diagram for the $\pi\pi$ S-wave amplitude in P-state annihilation.

How then does our fit reconcile the observations described at the opening of this subsection? The $f_0(1505)\pi^0$ peak lies almost on top of the intersection of the two $\rho(770)\pi$ bands and interferes constructively with them. This leads to the strong peak at $\sim$1515 MeV in $M_{\pi^+\pi^-}$. Our fit to the data in this region is essentially perfect, with no systematic discrepancies with the data. The situation for S-state annihilation to $\pi^+\pi^-\pi^0$ is that $^3S_1 \to \rho(770)\pi$ amplitudes are totally dominant, accounting for 85% of annihilation. They give a modest peak at the crossing of $\rho\pi$ bands, hence a rather small peak near A_X. The remaining 15% of $^1S_0$ annihilation makes a contribution too weak to give a significant $f_0(1505)$ signal. The appearance of the A_X peak in P-state annihilation but not in S-state annihilation to $\pi^+\pi^-\pi^0$ is therefore explained straightforwardly.

Having fitted P-state amplitudes to Asterix x-ray data, we can carry these amplitudes over to $3\pi^0$ (dropping the $^1P_1$ contributions, which are absent there). This enables us to estimate the fraction of P-state annihilation taking place in $\bar{p}p \to 3\pi^0$. The optimum fit gives 1% of P-state annihilation, with a χ^2 differing only by 5 from zero contribution. The fit is stable against forced introduction of P-state annihilation up to 5%. For this fraction, χ^2 has increased by 9% and is roughly parabolic with P-state fraction. Beyond this P-state fraction, the character of the fit changes qualitatively and χ^2 increases rapidly.

Suppose we introduce a large fraction of P-state annihilation, along the lines of Ref. [13]. There, no attempt was made to achieve consistency with the Asterix data. We have tried making a simultaneous fit to $3\pi^0$ and $\eta\eta\pi^0$ data with Asterix x-ray data, varying the strengths of amplitudes (62) to (71). Firstly, using the simple parametrization of the $\pi\pi$ S wave of Ref. [13], we cannot achieve any simultaneous fit with reasonable χ^2. The solution of

TABLE V. Intensities of contributions to $3\pi^0$ and $\eta\eta\pi^0$ data, normalized to 100% for the full amplitude squared. The first entry is for the $\pi\pi$ S wave excluding $f_0(1335)$ and $f_0(1505)$.

Channel	$3\pi^0$	$\eta\eta\pi^0$
$\pi\pi$ S wave	11.4	17.1
$f_0(1335)$	33.9	7.2
$f_0(1505)$	50.9	11.4
$f_2(1270)$	12.0	2.7
$f_2(1560)$	7.7	—
$a_0(980)$	—	19.1
$f_2(1525)$	—	0.40
Total	115.9	58.0

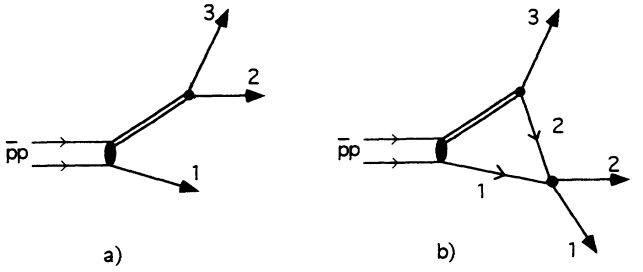

FIG. 22. The pole diagram in the 23 channel (a) and the corresponding triangle diagram (b).

Ref. [13] is therefore unsatisfactory. However, this situation is not a clean one. If the $\pi\pi$ S wave is given the more complicated form of Eq. (60), with five Λ parameters, there does exist sufficient flexibility to give a fit with a wide variety of large P-state fractions and with a χ^2 worse than for zero P state by only 25–50 %, depending on the precise parametrization. This ambiguity cannot be resolved definitively from data presently at our disposal. However, from simulations, we believe it could very probably be resolved by data on $\bar{p}n \to \pi^-\pi^0\pi^0$. There (i) the $\pi\pi$ S wave is present in only one channel and (ii) the $\rho(770)$ is present in the other two and acts as a powerful interferometer for both S-state and P-state contributions. We await these data with interest.

F. Branching ratios

Points of interest are the branching fractions of $f_0(1335)$ and $f_0(1505)$ to $\pi^0\pi^0$ and $\eta\eta$. In Table V we collect together the intensities of resonances and the $\pi\pi$ S wave from our compromise fit, Table III, integrated over the available phase space. The table is normalized to 100% for the total amplitude squared.

The branching ratios for $\bar{p}p \to 3\pi^0$ and $\bar{p}p \to \eta\eta\pi^0$ are, respectively, 6.8×10^{-3} [48] and 2×10^{-3} [13]. Normalizing to these values we find the branching ratios

$$\bar{p}p \to f_0(1335)\pi^0 \to \pi^0\pi^0\pi^0 = 22\times10^{-4} , \tag{72}$$

$$\bar{p}p \to f_0(1335)\pi^0 \to \eta\eta\pi^0 = 1.4\times10^{-4} , \tag{73}$$

$$\bar{p}p \to f_0(1505)\pi^0 \to \pi^0\pi^0\pi^0 = 33\times10^{-4} , \tag{74}$$

$$\bar{p}p \to f_0(1505)\pi^0 \to \eta\eta\pi^0 = 2.3\times10^{-4} . \tag{75}$$

As regards errors, the main difficulty is that there are strong interferences between amplitudes, particularly with the background $(\pi\pi)_S$ amplitude, both the piece below $s = 1.2$ GeV^2 and the parabolic background above $s = 1.2$ GeV^2. It is immediately evident from Table V that the individual contributions squared for $\eta\eta\pi^0$ add up to only 58% of the full amplitude squared. For $3\pi^0$, the corresponding total is 114%. In the case of $\eta\eta\pi^0$, there is another ambiguity. The background term $a+bs$ is large and could be in either $\pi\pi$ or $\pi\eta$. One cannot distinguish between these two possibilities since s_{12}, s_{23}, and s_{13} are linearly related and the mass range is limited. The consequence is an uncertainty in both $\pi\pi$ and $\eta\eta$ branching ratios of at least a factor 2. This is unfortunate, but unavoidable with present data. Our best estimates, subject to this proviso, are

$$\frac{f_0(1335)\to\eta\eta}{f_0(1335)\to\pi^0\pi^0} = 0.068 , \tag{76}$$

$$\frac{f_0(1505)\to\eta\eta}{f_0(1505)\to\pi^0\pi^0} = 0.075 . \tag{77}$$

In all fits, there is no doubt that both resonances decay dominantly to $\pi^0\pi^0$.

IV. TRIANGLE SINGULARITIES

We now turn to the triangle singularities of the form of Fig. 2. These were studied in the 1960s [22–24] and continue to attract interest [10–12]. The problem of the triangle singularity is part of a more general one: the problem of anomalous singularities in the physical region [4].

The triangle singularity can be calculated in a comparatively simple way with the use of Eqs. (13)–(15) if one substitutes for A_{23} (or A_{13}) the Breit-Wigner amplitude in Fig. 22(a):

$$A_{23} \to \frac{\mu}{M_R^2 - s_{23} - iM_R\Gamma} . \tag{78}$$

The triangle amplitude for the diagram of Fig. 22(b) is, using the same form as in Ref. [12] and putting $m_1 = m_2 = m_3 = m$,

$$A^{\mu}_{\rm Tr}(s_{12}) = \frac{is_{12}\mu}{\sqrt{P(s_{12})R(s_{12})}} \left\{ \ln \frac{(J_1 - s_{12})[R(s_{12}) + (s_{12} - s - m^2)(J_2 - s_{12}) + \sqrt{R(s_{12})R(J_2)}]}{(J_2 - s_{12})[R(s_{12}) + (s_{12} - s - m^2)(J_1 - s_{12}) + \sqrt{R(s_{12})R(J_1)}]} \right.$$

$$\left. + \ln \frac{2s_{12}(2m^2 - M^2) + s_{12}(s - m^2 - s_{12}) + \sqrt{R(s_{12})P(s_{12})}}{2s_{12}(2m^2 - M^2) + s_{12}(s - m^2 - s_{12}) - \sqrt{R(s_{12})P(s_{12})}} \right\} , \tag{79}$$

where

$$R(s_{12})=[(\sqrt{s}+m)^2-s_{12}][(\sqrt{s}-m)^2-s_{12}]\ ,$$
$$P(s_{12})=s_{12}(s_{12}-4m^2)\ , \tag{80}$$

and

$$J_{1,2}=2m^2+\tfrac{1}{2}(s-m^2-M^2)\mp\frac{1}{2M^2}\sqrt{P(M^2)R(M^2)} \tag{81}$$

with $M^2=M_R^2-iM_R\Gamma$.

The imaginary part of the first logarithm on the right-hand side of Eq. (79) is chosen such that $A^{\mu}_{\rm Tr}$ does not contain a singularity of the root type at the point $s_{12}=(\sqrt{s}-m)^2$ where $R(s_{12})$ vanishes. To this end, it is necessary that the phase of the expression under the logarithm vanishes at the point $s_{12}=(\sqrt{s}-m)^2$. We note that both logarithms in Eq. (79) have singularities at $s_{12}=J_1$ and $s_{12}=J_2$. But these singularities cancel each other on the first (physical) sheet. The logarithmic singularity $s_{12}=J_1$, located on the second sheet, occurs near the physical region at

$$(m+M_R)^2\le s\le m^2+2M_R^2\ . \tag{82}$$

It is located in the complex s_{12} plane below the physical region, in the same manner as Breit-Wigner resonances.

The locations of the triangle singularities are illustrated in Fig. 23. The solid line shows pole production in channel 23 and the dashed lines the corresponding triangle singularities. The latter intersect with the resonance where it crosses the edge of the Dalitz plot. Physically this arises because particle 2 of resonance 23 in Fig. 23(b) must correspond to forward or backward decay of the resonance, in order that it collides with the spectator 1. The sum of the two diagrams is given by

$$\frac{\mu}{s_{23}-M_R^2+i\Gamma M_R}+ie^{i\delta_{12}}\sin\delta_{12}A^{\mu}_{\rm Tr}(s_{12})\ . \tag{83}$$

Here δ_{12} is the phase shift for the scattering process $12\to12$. In Eq. (83) we redefine the constant μ, changing the sign of the pole diagram compared with Eq. (79); this new form is more suitable for our purposes.

The amplitude (83) satisfies the Schmid theorem [49]: it is integrated over z_{23} [see Eq. (15)]. Near the triangle singularity, $s_{12}\simeq J_1$, it is proportional to the factor $e^{2i\delta_{12}}$. So if we had a production amplitude containing only the two terms of Eq. (83), the effect on the one-particle spectrum (particle 3), would be the same as for the pole diagram alone. That is, there is a specific cancellation in the one-particle spectrum. However, if the production amplitude has other terms, as in Fig. 23, interference effects destroy this cancellation, and the triangle diagram will have some influence on the spectrum. Nevertheless, it will not be a large effect.

Now let us briefly discuss the properties of the triangle singularity. It is located at $s_{12}=J$ [see Eq. (79)]. This location can be easily found from the diagrams of Fig. 23, which we consider individually.

(i) For Fig. 23(a), the total energy is not large enough to produce the resonance in channel 23. The triangle singularity is far from the physical region.

(ii) For Fig. 23(b), the high mass resonance 23 is produced at its threshold. The triangle singularity appears near a value of s_{12} where the resonance touches the border of the Dalitz plot. Here we consider a resonance of small width.

(iii) In Fig. 23(c), the resonance is produced with some kinetic energy which is not very large. The position of the triangle singularity is determined by the point where the resonance crosses the lower edge of the Dalitz plot.

(iv) In Fig. 23(d), the singularity is near the threshold of channels 12 and 13. Finally in Fig. 23(e), resonance 23 is produced with large kinetic energy. The triangle singularity is now far from the Dalitz plot, i.e., far from the physical region of the reaction.

Summarizing, triangle singularities originate dominantly from high mass resonances, but the triangle singularities affect regions of lower s. Physically this corresponds to the fact that resonance s_{23} needs to decay in such a way that the decay particle can catch up with the spectator particle.

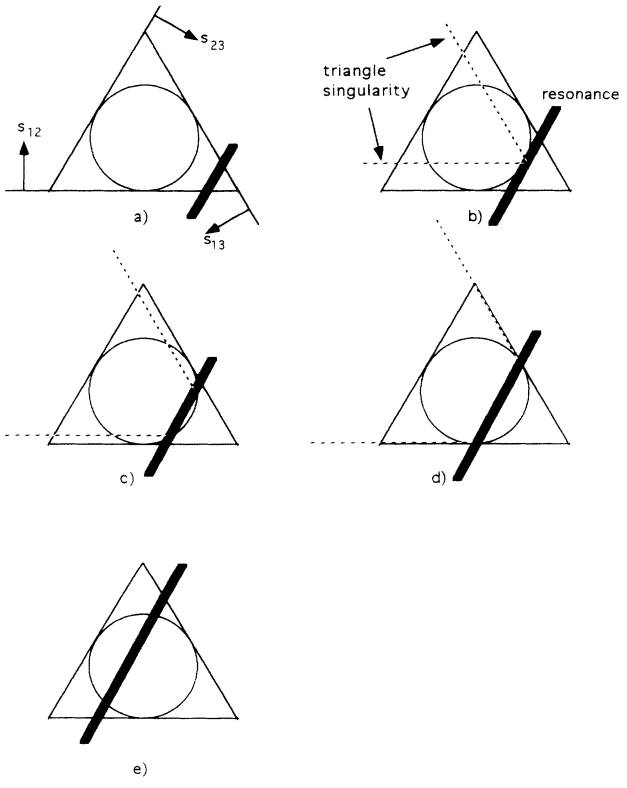

FIG. 23. The location of the triangle singularity near the physical region of the Dalitz plot (dashed line) depending on the position of the related resonance (solid line).

V. NUMERICAL RESULTS FOR THE TRIANGLE SINGULARITIES

In the calculation of the triangle diagrams we take into account the S-wave resonances $f_0(984-986)$ of Table I,

TABLE VI. Comparison of two sets of parameters with and without considering the triangle singularity.

Resonance	Parametrization without triangle singularity		Parametrization with triangle singularity	
	M	Γ	M	Γ
$f_0(1335)$	1.317	0.250	1.319	0.254
$f_0(1505)$	1.497	0.143	1.497	0.145
$f_2(1270)$	1.275	0.200	1.274	0.200
	$s_1=0.155$ $s_2=1.535$		$s_1=0.378$ $s_2=1.522$	
Low energy	$\gamma_1=3.545$ $\gamma_2=-3.728$		$\gamma_1=2.552$ $\gamma_2=-2.685$	
$\pi\pi$ S wave	$\gamma_3=1.765$ $\gamma_4=-1.291$		$\gamma_3=1.075$ $\gamma_4=-0.778$	
	$\gamma_5=-0.433$ $\gamma_6=1.134$		$\gamma_5=-0.516$ $\gamma_6=1.088$	
II-sheet pole	$M_1=0.984-i0.039$		$M_1=0.984-i0.036$	
III-sheet pole	$M_2=0.986-i0.102$		$M_2=0.980-i0.120$	
$\Lambda(1335)$	$0.4663-i0.7237$		$0.4862-i0.6542$	
$\Lambda(1505)$	$-0.3234-i0.6296$		$-0.3206-i0.6077$	
$\Lambda(1275)$	1.0		1.0	
Λ_1	$-8.1039+i5.3040$		$-3.7489+i5.9112$	
Λ_2	$8.9249-i4.8739$		$4.1848-i5.8031$	
Λ_3	$6.6132+i0.9599$		$4.3457+i1.1521$	
Λ_4	$-7.9705-i1.2337$		$-4.7535-i0.2612$	

form I, plus $f_0(1335)$ and $f_0(1505)$ and the D-wave resonance $f_2(1275)$. For S-wave resonances, Eq. (83) is used where μ is the residue in the position of the corresponding resonance. The centrifugal barrier should be taken into account for the triangle diagram with $f_2(1275)$: we substitute in this calculation $B_{J2}(s_{23},s_{12}) \rightarrow B_2[M^2(1275),J_1]$.

Results of calculations without triangle diagrams and with them are presented in Table VI. In this case, masses and widths change only slightly and likewise the poles of the low-energy S-wave $\pi\pi$ amplitude. This is no surprise because the low-energy S-wave $\pi\pi$ amplitude is mainly determined by data of Refs. [29–31], which were taken into account in both cases. The triangle singularities tend to affect the region of large energies less than low energies because in Fig. 23(e) triangle singularities are far from the physical region. The main changes are in the magnitudes of Λ parameters, particularly for the slowly varying $\pi\pi$ S wave. There is a considerable change in the phase of this amplitude ($\sim 25°$).

The Argand diagrams for the S-wave amplitude are shown in Fig. 24. Let us denote the S-wave amplitudes

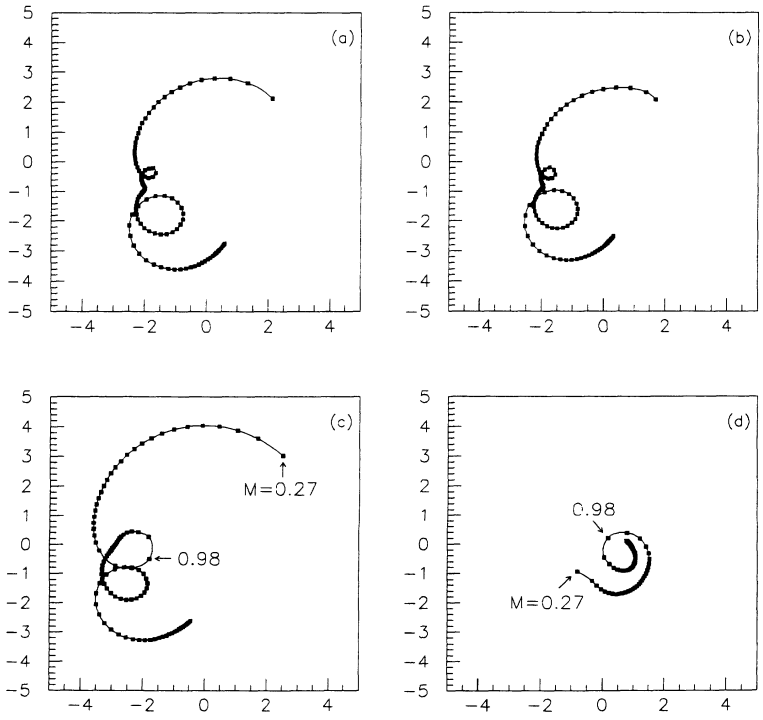

FIG. 24. Argand diagram for the S-wave $\pi\pi$ amplitude in $\bar{p}p \rightarrow 3\pi^0$ (a) for the fit without triangle diagrams; (b) with triangle diagrams, $A^{(\mathrm{tr})}$ Eq. (84); (c) for $A^{(\mathrm{tr})}_{\mathrm{res}}$; (d) for A_{tr}.

without the triangle diagram as $A(s)$ and with triangle diagram as $A^{(\mathrm{tr})}(s)$. Figures 24(a) and 24(b) show fits without and with triangle singularities. One can see that these two amplitudes practically coincide, i.e., the quality of the fit to the data is of the same quality either way. The amplitude $A^{(\mathrm{tr})}$ contains two contributions, resonance production and triangle diagram amplitudes

$$A^{(\mathrm{tr})}(s)=A^{(\mathrm{tr})}_{\mathrm{res}}(s)+A_{\mathrm{tr}}(s)\ , \tag{84}$$

$$A_{\mathrm{tr}}(s)=\frac{2}{3}\eta_0(s)\frac{e^{2i\delta(s)}-1}{2}A^{\mu}_{\mathrm{tr}}(s)\ ,$$

with δ and η_0 the isoscalar $\pi\pi$ S-wave phase shift and inelasticity; the factor $2/3$ is the isospin coefficient. The corresponding Argand diagrams for $A^{(\mathrm{tr})}_{\mathrm{res}}$ and A_{tr} are shown in Figs. 24(c) and 24(d). One can see that the circle which corresponds to the narrow resonance at 980 MeV becomes very visible in the Argand diagram for $A^{(\mathrm{tr})}_{\mathrm{res}}$. The rescattering diagrams shadow it to a considerable extent in Figs. 24(a) and 24(b).

VI. DISCUSSION AND CONCLUSION

We have shown that two fairly narrow resonances $f_0(1335)$ and $f_0(1505)$ are capable of fitting Crystal Barrel data on $p\bar{p}\to 3\pi^0$ and $\eta\eta\pi^0$. It is desirable to confront other data sets, notably CERN-Munich data, with this hypothesis.

The assumption in this analysis is that annihilation is dominated by the initial state $^1S_0$. The previous analysis interpreted $f_0(1505)$ instead as $A_X(1515)$ with $J^P=2^+$, but required a high fraction of P-state annihilation, namely, $\sim 60\%$. Our analysis is stable against small amounts of P-state contribution. Also our identification of $f_0(1505)$ is compatible with Asterix data on $p\bar{p}\to\pi^+\pi^-\pi^0$. If the P-state amplitudes from the latter are carried over to $p\bar{p}\to 3\pi^0$, the fraction of P-state annihilation in this reaction seems to be small, $\sim 1\%$. Further data on $\bar{p}n\to\pi^-\pi^0\pi^0$ at rest are likely to be helpful. Our analysis procedures are applicable to any process of three-body annihilation.

The lower resonance, $f_0(1335)$ is an obvious candidate for the $(u\bar{u}+d\bar{d})/\sqrt{2}$ member of the ground state 0^+ nonet in view of its similarity in mass to members of 1^{++}, 2^{++}, and 1^{+-} nonets. There is evidence for the $I=1$ partner $a_0(1415)$ [17,18,50]. A third candidate for the 0^{++} nonet is $K_0^*(1430)$ [51]. The $s\bar{s}$ member of the nonet is not well identified at present. The LASS Collaboration [51] has evidence for $f_0(1525)\to K^0K^0$ at a mass of 1525 MeV. Another potential candidate is $G(1590)$ of the GAMS Group [42]; this is claimed to have a strong $\eta\eta$ decay mode and an even stronger $\eta\eta'$ decay mode. It is a little surprising that $G(1590)$ does not show up in Crystal Barrel data. A better place to look will be in $p\bar{p}\to\pi^0(K\bar{K})$.

The $f_0(1505)$ does not fit naturally into a nonet, because of its strong $\pi\pi$ decay mode. The E760 Collaboration [52] sees a peak at 1500 MeV in $\pi^0\pi^0$ and $\eta\eta$ in $p\bar{p}\to 3\pi^0$ and $\eta\eta\pi^0$ at 3 to 3.5 GeV. The Crystal Barrel Collaboration also sees a narrow $\eta\eta$ peak at 1500 MeV in $p\bar{p}\to\eta\eta\pi^0$ at 1.94 GeV/c [53]. If $f_0(1505)$ were a radial excitation, such strong production would be surprising because of the node in the radial wave function. It is also anomalously low in mass for a radial excitation, which is expected at 1700–1800 MeV. We remark that Bridges *et al.* [54] claim that $\bar{p}n\to\pi^-X, X\to 4\pi$ is dominated by an $I=0$ resonance at 1500 MeV with $J^{PC}=0^{++}$ or 2^{++}, though they prefer 2^{++}.

An innocent explanation of $f_0(1505)$ or $A_X(1515)$ could be that it is associated with the $\rho\rho$ threshold, in the same way that $f_0(975)$ and $a_0(980)$ seem to be connected to the $K\bar{K}$ threshold and $f_0(1420)$ could be a KK^* molecule. However, there are arguments against this. Firstly, strong production of a molecule in E760 data is difficult to explain. A molecule especially implies a large radius (two $q\bar{q}$ pairs well separated) and should be suppressed by its form factor. Secondly, a molecule should be coupled to $(\rho\rho+\omega\omega)/\sqrt{2}$. The narrow width of $f_0(1505)$ is not easily reconciled with $\rho\rho$. Also there is no effect in the data at the $\omega\omega$ threshold, nor any $\omega\omega$ threshold enhancement in $p\bar{p}\to\omega\omega\pi^0$ at rest [55].

Finally we make a case for $f_0(1505)$ to be a glueball strongly mixed with $q\bar{q}$ in order to explain its strong $\pi\pi$ decay mode. A pure glueball state would be a color singlet and will have equal branching ratios to $\pi^0\pi^0$ and $\eta\eta$, except for a phase space factor q which favors $\pi\pi$ by about a factor of 1.3. One should look for a glueball in $J/\psi\to\gamma X$. We remark that there is indeed a peak in this reaction in $X\to 4\pi$ just at 1505 MeV, and with a width commensurate with what we find [56]. Published analyses find $J^p=0^-$, but this assignment deserves scrutiny. The analyses assume a pure $\rho\rho$ final state, but contribution from $\sigma\sigma$ might affect this conclusion. Branching ratios predicted for $\rho^0\rho^0$ and $\rho^+\rho^-$ disagree with the data. Also one must wonder why a 0^- state, which decays to $\rho\rho$ by $L=1$ should couple so strongly to $\rho\rho$ below its nominal threshold.

It is our opinion that the glueball hypothesis has to be taken seriously. The mass predicted by lattice gauge calculations is 1500 MeV [57], though in the quenched approximation.

ACKNOWLEDGMENTS

V.V.A. and A.V.S. are grateful to the SERC for financial assistance for a visit to QMW, London, in order to participate in the amplitude analysis. We acknowledge financial support from the UK Science and Engineering Research Council. We thank the Asterix Group for making available their gas data in numerical form. We thank Dr. K. Peters and Dr. I. Augustin for making available the Crystal Barrel data in numerical form. We are grateful to Dr. D. Morgan for extensive discussion about the $\pi\pi$ S wave.

[1] C. B. Dover *et al.*, Prog. Part. Nucl. Phys. **29**, 87 (1992); C. Amsler and F. Myhrer, Annu. Rev. Nucl. Part. Sci. **41**, 219 (1991).
[2] N. N. Khuri and S. B. Treiman, Phys. Rev. **119**, 1115 (1960).
[3] V. V. Anisovich, A.A. Anselm, and V. N. Gribov, Nucl. Phys. **38**, 132 (1962).
[4] P. V. Landshoff, Phys. Lett. **3**, 116 (1962).
[5] C. Kacser, Phys. Rev. **132**, 2712 (1963).
[6] V. V. Anisovich, Zh. Eksp. Teor. Fiz. **44**, 1593 (1963) [Sov. Phys. JETP **17**, 1072 (1963)].
[7] I. J. R. Aitchison, Phys. Rev. **137**, B1070 (1965).
[8] N. Isgur and G. Karl, Phys. Rev. D **19**, 2653 (1979); **20**, 1191 (1979).
[9] G. F. Chew and S. Mandelstam, Phys. Rev. **119**, 467 (1960).
[10] C. J. Goebel, S. F. Tuan, and W. A. Simmons, Phys. Rev. D **27**, 1069 (1983).
[11] X. He, S. Pakvosa, W. A. Simmons, and S. F. Tuan, Phys. Rev. D **31**, 2356 (1985).
[12] L. G. Dakhno, S. M. Sarasynta, and M. G. Kobrinsky, Yad. Fiz. **46**, 155 (1987) [Sov. J. Nucl. Phys. **46**, 96 (1987)].
[13] E. Aker *et al.*, Phys. Lett. B **260**, 249 (1991).
[14] C. Amsler *et al.*, Phys. Lett. B **291**, 347 (1992).
[15] A. Bettini *et al.*, Nuovo Cimento A **1**, 333 (1971).
[16] V. V. Anisovich *et al.*, Phys. Lett. B **323**, 233 (1994).
[17] V. V. Anisovich, "Proceedings of NAN Conference," Moscow, August 1993 (in press).
[18] D. V. Bugg, "Proceedings of Europhysics HEP Conference," Marseille, July 22–28, 1993 (in press).
[19] A. V. Anisovich and V. V. Anisovich, Yad. Fiz. **53**, 1485 (1991) [Sov. J. Nucl. Phys. **53**, 915 (1991).
[20] V. V. Anisovich, D.V. Bugg, and A. V. Sarantsev, Nucl. Phys. **A537**, 501 (1992).
[21] L. Castilejo, F. J. Dyson, and R. H. Dalitz, Phys. Rev. **101**, 45 (1956).
[22] I. J. R. Aitchison, Phys. Rev. **133**, 1257 (1964).
[23] B. N. Valuev, Zh. Eksp. Teor. Fiz. **47**, 649 (1964) [Sov. Phys. JETP **20**, 433 (1965)].
[24] V. V. Anisovich and L. G. Dakhno, Phys. Lett. **10**, 221 (1964); Nucl. Phys. **76**, 665 (1966).
[25] A. V. Anisovich, "Dispersion Relation Techniques for Three-Pion Systems and *P*-Wave Interaction in $\eta \to 3\pi$ Decay," Report No. PNPI-93, St. Petersburg, 1993 (unpublished).
[26] C. Lovelace, Phys. Lett. **28B**, 264 (1968).
[27] R. Odorico, Phys. Lett. **33B**, 489 (1970).
[28] S. M. Flatté, Phys. Lett. **63B**, 224 (1976).
[29] L. Rosselet *et al.*, Phys. Rev. D **15**, 574 (1977).
[30] G. Grayer *et al.*, Nucl. Phys. **B75**, 189 (1974).
[31] W. Ochs, University of Munich, Ph.D. thesis, 1974.
[32] Particle Data Group, K. Hikasa *et al.*, Phys. Rev. D **45**, S1 (1992).
[33] K. L. Au, D. Morgan, and M. R. Pennington, Phys. Rev. D **35**, 1633 (1987).
[34] A. Donnachie and A. B. Clegg, Z. Phys. C **51**, 689 (1991).
[35] T. A. Armstrong *et al.*, Z. Phys. C **51**, 351 (1991).
[36] R. H. Dalitz and S. Tuan, Ann. Phys. (N.Y.) **10**, 307 (1960).
[37] B. S. Zou and D. V. Bugg, Phys. Rev. D **48**, 3948 (1993).
[38] M. Alston-Garnjost *et al.*, Phys. Lett. **36B**, 152 (1971).
[39] W. Lockman, in *The Hadron Mass Spectrum,* Proceedings of the Conference, St. Goar, Germany, 1990, edited by E. Klempt and K. Peters [Nucl. Phys. B (Proc. Suppl.) **21**, 55 (1991)].
[40] L. P. Chen *et al.*, in *Hadron' 91,* Proceedings of the Fourth International Conference on Hadron Spectroscopy, College Park, Maryland, 1991, edited by S. Oneda and D. C. Peaslee (World Scientific, Singapore, 1992), p. 111.
[41] T. A. Armstrong *et al.*, Phys. Lett. B **227**, 185 (1989).
[42] F. Binon *et al.*, Nuovo Cimento A **38**, 313 (1983); **80**, 363 (1984); D. Alde *et al.*, Nucl. Phys. **B269**, 485 (1986); D. Alde *et al.*, Phys. Lett. B **201**, 160 (1988).
[43] Particle Data Group [32], the tensor-meson sector, p. VII.194.
[44] W. Ochs (private commnication).
[45] B. Hyams *et al.*, Nucl. Phys. **B64**, 134 (1973), Fig. 1.
[46] J. Vandermeulen, Z. Phys. C **37**, 563 (1988).
[47] B. May *et al.*, Z. Phys. C **46**, 203 (1990).
[48] B. May *et al.*, Z. Phys. C **46**, 191 (1990).
[49] C. Schmid, Phys. Rev. **154**, 154 (1967).
[50] V. V. Anisovich, D. V. Bugg, A.V. Sarantsev, and B. S. Zou, QMW report, 1993 (unpublished).
[51] D. Aston *et al.*, Nucl. Phys. **B296**, 493 (1988); M. Baubillier *et al.*, Z. Phys. C **17**, 309 (1983).
[52] T. A. Armstrong *et al.*, Phys. Lett. B **307**, 399 (1993).
[53] K. Peters (private communication).
[54] D. Bridges, I. Daftari, and T. E. Kalogeropoulos, Phys. Rev. Lett. **57**, 1534 (1986).
[55] C. Strassburger (private communication).
[56] R. M. Baltrusaitis *et al.*, Phys. Rev. D **33**, 1222 (1986); D. Bisello *et al.*, *ibid.* **39**, 701 (1989).
[57] G. S. Bali *et al.*, Phys. Lett. B **309**, 378 (1993).

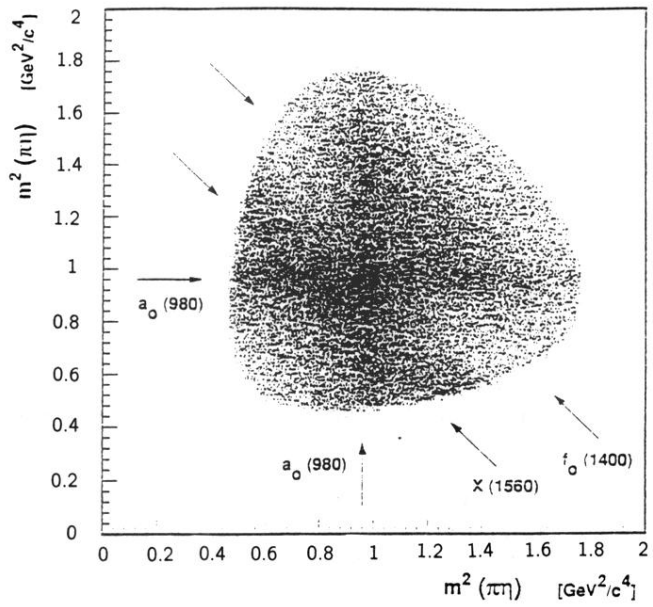

FIG. 11. Dalitz plot for $\bar{p}p \to \eta\eta\pi^0$ at rest, reproduced from Ref. [14].